Tanaka, M., Schinke, M., Liao, H. S., Yamasaki, N., & Izumo, S. (2001). Nkx2.5 and Nkx2.6, homologs of *Drosophila* tinman, are required for development of the pharynx. *Mol Cell Biol 21*, 4391–4398.

Terami, H., Hidaka, K., Katsumata, T., Iio, A., & Morisaki, T. (2004). Wnt11 facilitates embryonic stem cell differentiation to Nkx2.5-positive cardiomyocytes. *Biochem Biophys Res Commun 325*, 968–975.

Thattaliyath, B. D., Firulli, B. A., & Firulli, A. B. (2002). The basic helix-loop-helix transcription factor HAND2 directly regulates transcription of the atrial naturetic peptide gene. *J Mol Cell Cardiol 34*, 1335–1344.

Thomas, P. S., Kasahara, H., Edmonson, A. M., Izumo, S., Yacoub, M. H., Barton, P. J., et al. (2001). Elevated expression of Nkx-2.5 in developing myocardial conduction cells. *Anat Rec 263*, 307–313.

Thompson, J. T., Rackley, M. S., & O'Brien, T. X. (1998). Upregulation of the cardiac homeobox gene Nkx2-5 (CSX) in feline right ventricular pressure overload. *Am J Physiol 274*, H1569–H1573.

Toko, H., Zhu, W., Takimoto, E., Shiojima, I., Hiroi, Y., Zou, Y., et al. (2002). Csx/Nkx2-5 is required for homeostasis and survival of cardiac myocytes in the adult heart. *J Biol Chem 277*, 24735–24743.

Tonissen, K. F., Drysdale, T. A., Lints, T. J., Harvey, R. P., & Krieg, P. A. (1994). XNkx- 2.5, a *Xenopus* gene related to Nkx-2.5 and tinman: evidence for a conserved role in cardiac development. *Dev Biol 162*, 325–328.

Turbay, D., Wechsler, S. B., Blanchard, K. M., & Izumo, S. (1996). Molecular cloning, chromosomal mapping, and characterization of the human cardiac-specific homeobox gene hCsx. *Mol Med 2*, 86–96.

Tzahor, E., & Lassar, A. B. (2001). Wnt signals from the neural tube block ectopic cardiogenesis. *Genes Dev 15*, 255–260.

Ueyama, T., Kasahara, H., Ishiwata, T., Nie, Q., & Izumo, S. (2003a). Myocardin expression is regulated by Nkx2.5, and its function is required for cardiomyogenesis. *Mol Cell Biol 23*, 9222–9232.

Ueyama, T., Kasahara, H., Ishiwata, T., Yamasaki, N., & Izumo, S. (2003b). Csm, a cardiac-specific isoform of the RNA helicase Mov10l1, is regulated by Nkx2.5 in embryonic heart. *J Biol Chem 278*, 28750–28757.

Veeman, M. T., Axelrod, J. D., & Moon, R. T. (2003). A second canon. Functions and mechanisms of beta-catenin-independent Wnt signaling. *Dev Cell 5*, 367–377.

von Both, I., Silvestri, C., Erdemir, T., Lickert, H., Walls, J. R., Henkelman, R. M., et al. (2004). Foxh1 is essential for development of the anterior heart field. *Dev Cell 7*, 331–345.

Watanabe, Y., Benson, D. W., Yano, S., Akagi, T., Yoshino, M., & Murray, J. C. (2002). Two novel frameshift mutations in NKX2.5 result in novel features including visceral inversus and sinus venosus type ASD. *J Med Genet 39*, 807–811.

Winnier, G., Blessing, M., Labosky, P. A., & Hogan, B. L. (1995). Bone morphogenetic protein-4 is required for mesoderm formation and patterning in the mouse. *Genes Dev 9*, 2105–2116.

Wu, X., Golden, K., & Bodmer, R. (1995). Heart development in *Drosophila* requires the segment polarity gene wingless. *Dev Biol 169*, 619–628.

Xu, X., Yin, Z., Hudson, J. B., Ferguson, E. L., & Frasch, M. (1998). Smad proteins act in combination with synergistic and antagonistic regulators to target Dpp responses to the *Drosophila* mesoderm. *Genes Dev 12*, 2354–2370.

Yamagishi, H., Yamagishi, C., Nakagawa, O., Harvey, R. P., Olson, E. N., & Srivastava, D. (2001). The combinatorial activities of Nkx2.5 and dHAND are essential for cardiac ventricle formation. *Dev Biol 239*, 190–203.

Yamaguchi, K., Shirakabe, K., Shibuya, H., Irie, K., Oishi, I., Ueno, N., et al. (1995). Identification of a member of the MAPKKK family as a potential mediator of TGF-beta signal transduction. *Science 270*, 2008–2011.

Zhang, H., & Bradley, A. (1996). Mice deficient for BMP2 are nonviable and have defects in amnion/chorion and cardiac development. *Development 122*, 2977–2986.

Zhu, W., Shiojima, I., Hiroi, Y., Zou, Y., Akazawa, H., Mizukami, M., et al. (2000). Functional analyses of three Csx/Nkx-2.5 mutations that cause human congenital heart disease. *J Biol Chem 275*, 35291–35296.

Zou, Y., Evans, S., Chen, J., Kuo, H. C., Harvey, R. P., & Chien, K. R. (1997). CARP, a cardiac ankyrin repeat protein, is downstream in the Nkx2-5 homeobox gene pathway. *Development 124*, 793–804.

Kir6.2-deficient mice are susceptible to stimulated ANP secretion: K_{ATP} channel acts as a negative feedback mechanism?

Noriko Saegusa[a,b], Toshiaki Sato[a], Tomoaki Saito[a], Masaji Tamagawa[a], Issei Komuro[b], Haruaki Nakaya[a,*]

[a]*Department of Pharmacology, Chiba University Graduate School of Medicine, 1-8-1 Inohana, Chuo-ku, Chiba 260-8670, Japan*
[b]*Department of Cardiovascular Science and Medicine, Chiba University Graduate School of Medicine, 1-8-1 Inohana, Chuo-ku, Chiba 260-8670, Japan*

Abstract

Objective: While atrial natriuretic peptide (ANP) has been shown to be released mainly from cardiac muscle cells in response to atrial distension, the regulatory mechanisms of ANP secretion are still not fully understood. We sought to determine whether the ATP-sensitive K^+ (K_{ATP}) channel modulates the secretion of ANP, using mice with homozygous knockout of the Kir6.2 (a pore-forming subunit of cardiac K_{ATP} channel) gene.
Methods: K_{ATP} channel currents were recorded from isolated mouse atrial cells with patch–clamp techniques. Plasma ANP concentrations in anesthetized mice and ANP content and secretion in isolated atrial preparations were determined by radioimmunoassay. Action potentials were recorded from the isolated atria.
Results: Exposure to 2,4-dinitrophenol (100 µM) evoked a glibenclamide-sensitive K_{ATP} channel current in atrial cells from wild-type (WT) but not Kir6.2 knockout (Kir6.2 KO) mice. Although there were no significant differences in the basal plasma ANP levels between WT and Kir6.2 KO mice, volume expansion caused a significant elevation of plasma ANP concentration in Kir6.2 KO but not WT mice with accompanying hypotension. When isolated left atria were stretched, ANP secreted into the bath from Kir6.2 KO atria was significantly higher than that from WT atria. Furthermore, stretching the atria from WT but not Kir6.2 KO mice significantly shortened the action potential duration. A hypotonic stretch of the membrane induced the glibenclamide-sensitive K_{ATP} channel current in atrial cells from WT but not Kir6.2 KO mice.
Conclusions: Kir6.2 is essential for the function of K_{ATP} channel in mouse atrial cells. Given that Kir6.2 KO mice are susceptible to stretch-induced secretion of ANP, our results suggest that K_{ATP} channels may act as a negative feedback mechanism for the control of ANP secretion.
© 2005 European Society of Cardiology. Published by Elsevier B.V. All rights reserved.

Keywords: Natriuretic peptide; K-ATP channel; Myocytes

This article is referred to in the Editorial by L.G. Bianciotti (pages 9–10) in this issue.

1. Introduction

ATP-sensitive K^+ (K_{ATP}) channels, originally discovered in cardiac muscle [1], are present in many tissues and play an important role in various cellular responses [2]. The molecular identity of sarcolemmal K_{ATP} channels is now known to be a hetero-octameric complex of four pore-forming subunits (Kir6.x) and four sulfonylurea receptor regulatory subunits (SUR) [2]. Previous studies have shown that mutant mice lacking the Kir6.2 subunit of K_{ATP} channels (Kir6.2 KO mice) display obvious impairment of insulin response to glucose [3] and are susceptible to generalized seizures after brief hypoxia [4]. Our recent studies using the Kir6.2 KO mice have provided direct evidence that Kir6.2 forms the pore region of ventricular K_{ATP} channels [5] and the activation of K_{ATP} channels plays an important role in cardioprotection [6]. More recently, Kir6.2 KO mouse models highlight the importance of K_{ATP} channels in adaptation to stress beyond their role in cytoprotection [7].

---

* Corresponding author. Tel.: +81 43 226 2051; fax: +81 43 226 2052.
E-mail address: nakaya@faculty.chiba-u.jp (H. Nakaya).

Although considerable advances have been made in recent years towards understanding the nature of ventricular K_{ATP} channels, the molecular identity and functional role of atrial K_{ATP} channels are poorly understood. Atrial distention causes release into the circulation of atrial natriuretic peptide (ANP), a hormone that plays a role in the regulation of cardiovascular homeostasis [8]. Since the gating of the atrial K_{ATP} channel is mechanosensitive [9], the relationship to the process of ANP secretion is a subject of considerable interest. Kim et al. [10] reported that the K_{ATP} channel blocker glibenclamide suppressed the stretch-stimulated ANP secretion from rat atria. On the other hand, conflicting observation was reported that the K_{ATP} channel blocker tolbutamide increased the release of ANP in neonatal rat atrial myocytes [11]. Moreover, Xu et al. [12] reported that the stretch-induced ANP secretion was inhibited by K_{ATP} channel openers. Thus, the results so far obtained by using K_{ATP} channel blockers and openers are not conclusive. In this study, we sought to determine whether atrial K_{ATP} channel regulates the secretion of ANP, using Kir6.2-deficient mice. The results show that Kir6.2 is essential for the function of atrial K_{ATP} channel and Kir6.2-deficient mice are susceptible to stretch-induced secretion of ANP.

2. Methods

2.1. Kir6.2-deficient mice

All procedures were performed in conformity with the Guide for the Care and Use of Laboratory Animals (NIH publication No. 85-23, revised 1996) and were approved by the Institutional Animal Care and Use Committee of Chiba University. A mouse line deficient in the K_{ATP} channels was generated by targeted disruption of the gene coding for Kir6.2, as described previously [3]. C57BL/6 mice were used as control because they had been back-crossed to a C57BL/6 strain for five generations. Twelve- to fourteen-week-old Kir6.2-deficient mice or C57BL/6 control mice were used in this study.

2.2. Electrophysiology

Single atrial cells were enzymatically isolated by the method of Suzuki et al. [5] with some modifications. Single-channel and whole-cell membrane currents were recorded by the patch–clamp method as previously described [5,6]. Whole-cell current recordings were performed at 36 °C with nystatin in the pipette solution. Single atrial cells were superfused with HEPES–Tyrode's solution (in mM): NaCl 143, KCl 5.4, CaCl$_2$ 1.8, MgCl$_2$ 0.5, NaH$_2$PO$_4$ 0.33, glucose 5.5, and HEPES–NaOH buffer 10 (pH=7.4). The pipette solution contained (in mM): K-aspartate 110, KCl 20, MgCl$_2$ 1.0, CaCl$_2$ 1.0, EGTA 0.1, and HEPES–KOH buffer 5 (pH=7.4), with 250 µg/ml nystatin. A ramp-pulse protocol (−100 to +50 mV over 2.5 s, repeated at 30-s

intervals) was used to record the quasi-steady-state membrane current. For the experiments of hypotonic stretch of the membrane (Fig. 6), the isolated atrial cells were exposed to the low-chloride isotonic or hypotonic solution in order to minimize swelling-induced chloride current contamination [13]. Isotonic solution contained (in mM): Na-aspartate 80, KCl 5.4, CaCl$_2$ 1.8, MgCl$_2$ 0.5, NaH$_2$PO$_4$ 0.33, glucose 5.5, mannitol 119, and HEPES–NaOH buffer 10 (pH=7.4, ≈36 °C) with an osmolarity of 300 mosM/kg H$_2$O. Hypotonic solution was prepared by simply omitting mannitol from the isotonic solution with the osmolality of 180 mosM/kg H$_2$O. For single-channel recordings from the cell-attached patches, symmetrical high K$^+$ external and internal solutions (≈22 °C) were used. The external solution contained (in mM): KCl 140, EGTA 5, Na$_2$–ATP 0.1, and HEPES–KOH buffer 5 (pH=7.4) and the pipette solution contained (in mM): KCl 140, MgCl$_2$ 1.8, CaCl$_2$ 1.8, and HEPES–KOH buffer 5 (pH=7.4). The current signals were digitized at 2 kHz for data analysis with pClamp software (Axon Instruments, Foster City, CA).

2.3. Volume expansion

The mice were anesthetized with urethane (1.5 g/kg, i.p.) and placed on a heating pad to maintain rectal temperatures at 37 °C. The left external jugular vein was cannulated with small polyethylene catheters for intravenous infusion. Volume expansion was performed by a modification of the method of Kishimoto et al. [14]. The lactated Ringer's solution containing 4.5% bovine serum albumin was infused at a rate of 200 µl/h/g (body weight) for 30 min. The rate of infusion was then lowered to 4.3 µl/h/g for another 30 min. In some experiments the initial infusion rate was increased from 200 to 400 µl/h/g for 30 min, after which the infusion was continued at a rate of 4.3 µl/h/g for 30 min. These infusions were carried out with a microinfusion pump (Harvard Apparatus, MA). At the end of the volume expansion, blood (700 µl) was drawn from the right carotid artery, collected into a tube containing EDTA and aprotinin, and centrifuged for 20 min at 4 °C. Plasma samples were stored at −80 °C until analysis by ANP radioimmunoassay.

2.4. Hemodynamic measurements

Arterial blood pressure was measured continuously in mice anesthetized with urethane. The right carotid artery was cannulated with small polyethylene catheters for the measurement of blood pressure via a pressure transducer. Heart rate was derived from the arterial blood pressure signal.

2.5. Isolated atrial preparations

Tissue bath preparations of left atria were prepared by a modification of the method described by Bilder et al. [15].

Briefly, left atria from WT and Kir6.2 KO mice were dissected free and placed in a 3-ml water jacketed tissue bath containing HEPES–Tyrode's solution (pH=7.4) gassed with 100% O_2 (37 °C). The edge of preparation was pinned to the rubber base of the tissue bath and electrically paced at a frequency of 5 Hz. After 10 min equilibration, the bath solution was discarded and 1 ml of fresh HEPES–Tyrode's solution was added to the bath. Atrial preparations were incubated in this solution with or without stretch stimulus. The atria connected to a string were stretched with a fixed resting tension of 0.5 g. After 10 min of incubation, the bath solution was collected into a tube containing EDTA and aprotinin and was stored at −80 °C until analysis by ANP radioimmunoassay.

2.6. ANP content of the atria

The hearts were rapidly removed from the anesthetized mice and the left atria were dissected out and immediately frozen in liquid nitrogen. The lysates were obtained from three preparations by homogenization in ice-cold buffer (0.1 mM acetic acid). The lysates were incubated for 8 min at 100 °C, kept on ice for 15 min and cleared by centrifugation at $66,000 \times g$ for 20 min at 4 °C. Protein concentration was determined by the BCA protein assay kit (PIERCE, Rockford, IL).

2.7. ANP radioimmunoassay

The concentration of immunoreactive ANP was measured by commercially available radioimmunoassay, as described previously [16]. The threshold for detection of ANP was 1.5 pg/ml.

2.8. Action potential recordings

The preparations of left atria from WT and Kir6.2 KO mice were mounted in a recording chamber and perfused at a constant flow (5 ml/min) with Tyrode's solution (in mM): NaCl 125, KCl 4.0, $CaCl_2$ 2.7, $MgCl_2$ 0.5, NaH_2PO_4 1.8, glucose 5.5, and $NaHCO_3$ 25 and gassed with 95% O_2/5% CO_2 (37 °C). Action potentials were evoked by electrical field stimulation at 5 Hz (2-ms rectangular pulses at $2 \times$ threshold intensity) and recorded by use of a 3 M KCl-filled microelectrode (tip resistance 10–20 MΩ). The edge of left atrial preparation was stretched with a fixed resting tension of 0.5 g. Transmembrane potential was recorded by a direct current preamplifier (MEZ-7200, Nihon Kohden, Tokyo, Japan) and digitized (PowerLab 2/20, ADInstruments, Castle Hill, Australia).

2.9. Drugs

The following drugs were used: nystatin (Wako Pure Chemicals, Osaka, Japan) and glibenclamide (Sigma-Aldrich Japan, Tokyo, Japan). Nystatin was dissolved in

methanol at a concentration of 10 mg/ml and added to the pipette solution at a concentration of 250 μg/ml just before experiments. Glibenclamide was dissolved in dimethyl sulfoxide as a stock solution of 10 mM and final concentration of dimethyl sulfoxide was less than 0.1%.

2.10. Statistics

All data are presented as mean±SEM. Statistical comparisons were made with the use of Student's t test or ANOVA combined with Fisher post hoc test, as appropriate. A p value of less than 0.05 was considered significant.

3. Results

3.1. K_{ATP} channel function in atrial cells

We first evaluated K_{ATP} channel function in atrial cells isolated from wild-type (WT) and Kir6.2-deficient (Kir6.2 KO) mice. Whole-cell membrane currents were recorded using a ramp-pulse protocol (Fig. 1A and B). There were no significant differences in the density of the outward current at 0 mV between atrial cells isolated from WT (1.4±0.1 pA/pF, $n=6$) and Kir6.2 KO mice (1.6±0.1 pA/pF, $n=6$) in the control condition. In WT cells, metabolic inhibition with a glucose-free, 100 μM DNP-containing solution induced an outward current (9.1±0.1 pA/pF at 0 mV, $n=6$), which, by virtue of its blockade by 1 μM glibenclamide (1.3±0.1 pA/pF, $n=6$), was confirmed to be the K_{ATP} current. However, such a membrane current change was not observed in Kir6.2 KO cells (1.6±0.1 pA/ pF after metabolic inhibition, $n=6$). When the atrial cells were exposed to a solution containing DNP (100 μM), single K_{ATP} channel activity could be recorded from 25 of 25 cell-attached patches of 9 WT mice (Fig. 1C). The channel openings were inhibited by addition of 1 μM glibenclamide to the solution (data not shown). The linear slope conductance, obtained from the current–voltage relationship from −100 to −40 mV for the single channel current of WT cells, was 71.6±1.7 pS ($n=7$). In contrast, opening of K_{ATP} channels could not be recorded from any cell-attached patches of Kir6.2 KO cells ($n=18$). These results indicate that Kir6.2 is essential for the function of K_{ATP} channel in atrial cells.

3.2. Effect of volume expansion on plasma ANP level

In anesthetized mice, there were no significant differences in the basal plasma ANP concentrations between WT (28.7±3.0 pg/ml, $n=7$) and Kir6.2 KO mice (36.6±4.9 pg/ ml, $n=6$). After volume expansion (200 μl/h/g for 30 min and 4.3 μl/h/g for another 30 min), the plasma ANP level was increased to 31.8±1.6 pg/ml ($n=7$) in WT mice, but this change was not statistically significant ($p=0.385$ vs. baseline). On the other hand, Kir6.2 KO mice reacted to
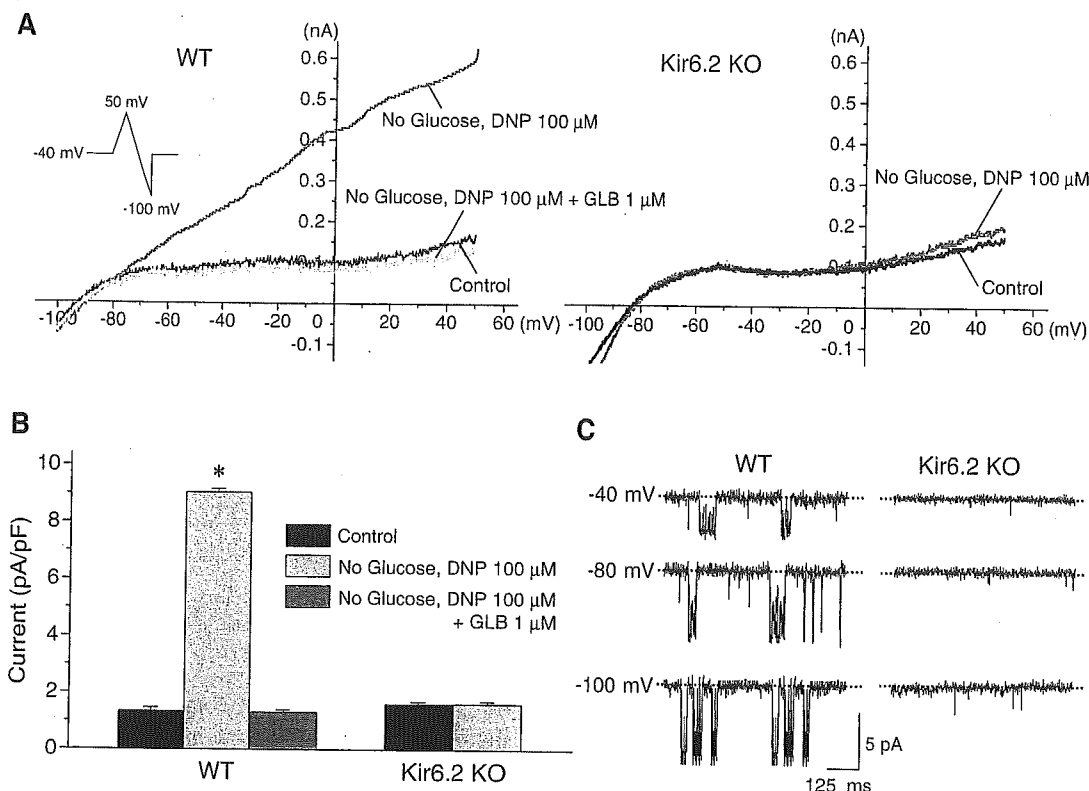
Fig. 1. (A) Effect of metabolic inhibition with a glucose-free, DNP-containing (100 μM) solution and co-application of glibenclamide (GLB, 1 μM) on the nystatin-perforated whole-cell membrane currents recorded from atrial cells of WT (left) and Kir6.2 KO mice (right). (B) Current densities at 0 mV from control ($n = 6$ of WT, $n = 6$ of Kir6.2 KO, black bar), DNP-treated ($n = 6$ of WT, $n = 6$ of Kir6.2 KO, grey bar) and DNP+GLB ($n = 6$ of WT, dark grey bar) mice of atrial cells are summarized. Values are mean±SEM. $*p < 0.01$ vs. control. (C) Single-channel current recordings in the cell-attached mode by addition of DNP (100 μM) from atrial cells of WT (left) and Kir6.2 KO mice (right). The test potential is indicated on the left.

volume expansion and the plasma ANP concentration significantly increased to 73.5±13.4 pg/ml ($n=5$, $p=0.021$ vs. baseline). The elevation of plasma ANP levels observed in Kir6.2 KO mice was notably higher than that observed in WT mice ($p=0.004$, Fig. 2). When the initial infusion rate was increased from 200 to 400 μl/h/g for 30 min (then the rate of infusion was lowered to 4.3 μl/h/g for 30 min) to give a severe volume expansion, the plasma ANP concentration in WT mice significantly increased to 49.8±8.2 pg/ml ($n=4$, $p=0.024$ vs. baseline). This value was not significantly different from that in Kir6.2 KO mice (53.9±4.9 pg/ml, $n=4$). These results indicate that Kir6.2 KO mice are susceptible to the ANP secretion by volume expansion.

3.3. Hemodynamic effects of volume expansion

There were no significant differences in the basal values of mean arterial pressure (MAP) between WT and Kir6.2 KO mice (Fig. 3). The values of MAP at 30 min of volume expansion were similarly increased in both WT (112.0± 4.1% of baseline, $n=4$) and Kir6.2 KO mice (111.3±2.3% of baseline, $n=4$). In WT mice, MAP returned to baseline
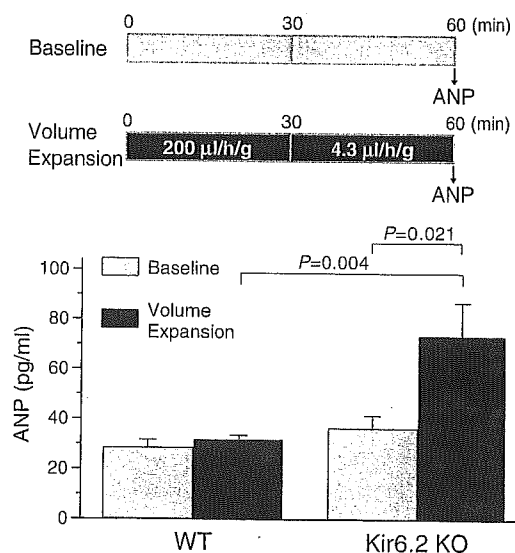

Fig. 2. Effect of volume expansion on plasma ANP levels of WT and Kir6.2 KO mice. Top panel shows the experimental protocol. Bottom panel shows summarized data for plasma ANP concentration. Blood samples were drawn at baseline ($n=7$ of WT, $n=6$ of Kir6.2 KO, grey bar) and after volume expansion ($n=7$ of WT, $n=5$ of Kir6.2 KO, black bar). Values are mean±SEM.
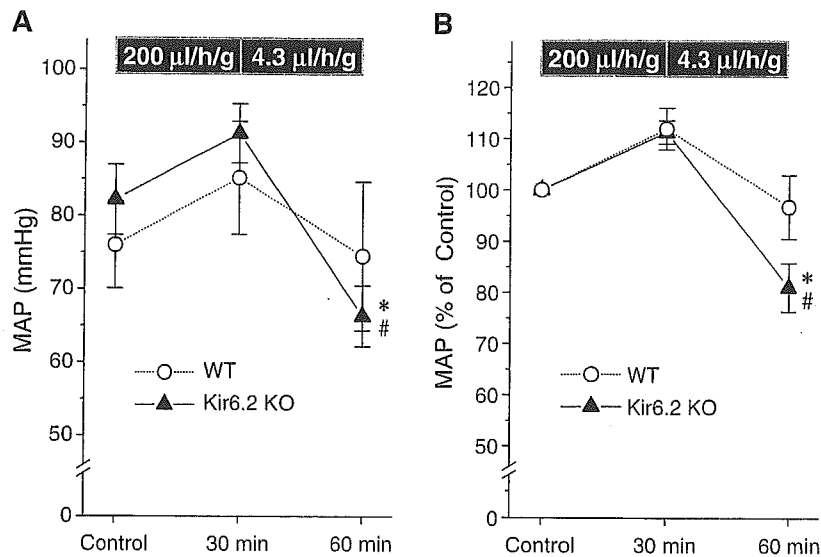
Fig. 3. Effect of volume expansion on mean arterial pressure (MAP) in anesthetized mice. (A) Changes of MAP before (baseline) and after 30 and 60 min of volume expansion. (B) MAPs are given as a percentage of the value measured at baseline. Data represent mean±SEM of 4 experiments for each group. $*p < 0.05$ vs. baseline, $\#p < 0.05$ vs. 30 min.

levels after 60 min of volume expansion ($96.7 \pm 6.2\%$ of baseline, $n = 4$). In contrast, 60 min of volume expansion in the Kir6.2 KO mice produced significant decrease in MAP ($81.0 \pm 4.7\%$ of baseline, $n = 4$, $p < 0.05$). There were no significant differences in the basal values of heart rate between WT (654 ± 31 bpm, $n = 7$) and Kir6.2 KO mice (642 ± 50 bpm, $n = 5$). Volume expansion did not alter the heart rate in both WT (689 ± 25 bpm, $n = 7$) and Kir6.2 KO mice (644 ± 50 bpm, $n = 5$).

3.4. ANP secretion from isolated atria

Isolated mouse atrial preparations were used to study the direct effect of mechanical stretch on ANP release. As shown in Fig. 4, in most cases the ANP concentration did
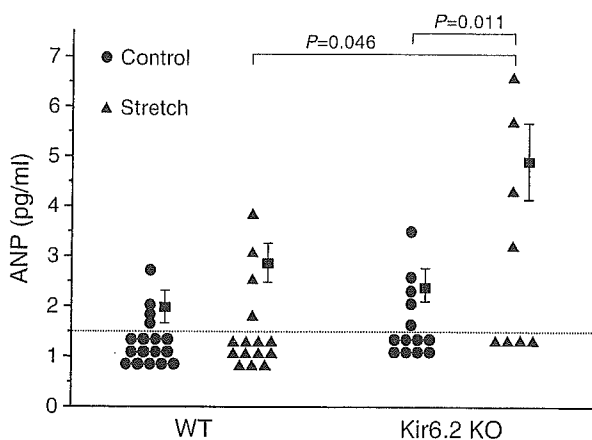

Fig. 4. Effects of mechanical stretch on ANP secretion in isolated atria from WT and Kir6.2 KO mice. The threshold for detection of ANP (1.5 pg/ml) is represented as dotted line. Each symbol represents data from individual preparations. Closed squares indicate the mean and the vertical bars indicate SEM.

not exceed the threshold for detection (≥ 1.5 pg/ml). We therefore repeated the experiment until the ANP secretion was detected in 4 or 5 of the preparations in each group. In control (non-stretch) conditions, ANP secretion was detected in 4 of 17 atria from WT and in 5 of 13 atria from Kir6.2 KO, respectively. The mean ANP concentration in each of 4 or 5 preparations (WT: 2.2 ± 0.2 pg/ml, Kir6.2 KO: 2.8 ± 0.4 pg/ml) was not statistically significant. After mechanical stretch for 10 min, ANP secretion was detected in 4 of 15 atria from WT. In Kir6.2 KO atria, ANP secretion was detected in 4 of 8 preparations and the mean ANP concentration (4.9 ± 0.7 pg/ml) was notably higher that that observed in WT atria (2.4 ± 0.3 pg/ml, $p = 0.046$).

ANP content of atria obtained from WT and Kir6.2 KO mice was 0.64 ± 0.30 ng/mg protein and 0.74 ± 0.23 ng/mg protein, respectively; these values did not reach statistical significance ($n = 3$, $p = 0.696$).

3.5. Action potentials in isolated atria

Representative recordings of action potentials before and after 5 min of stretch are shown in Fig. 5A and B. The action potential duration (APD) in the WT atrium was shortened at 5 min of stretch, while the APD remained unaltered in the Kir6.2 KO atrium. As summarized in Fig. 5C, stretching the WT atria significantly shortened the APD measured at 90% repolarization (APD_{90}) to $71.8 \pm 3.4\%$ of control ($n = 4$, $p = 0.004$). Stretch-induced shortening of APD_{90} was not observed in Kir6.2 KO atria ($98.6 \pm 0.7\%$, $n = 4$).

3.6. Hypotonic stretch-induced K_{ATP} current

To determine whether K_{ATP} channel currents could be mechanically induced, the nystatin-perforated patch was
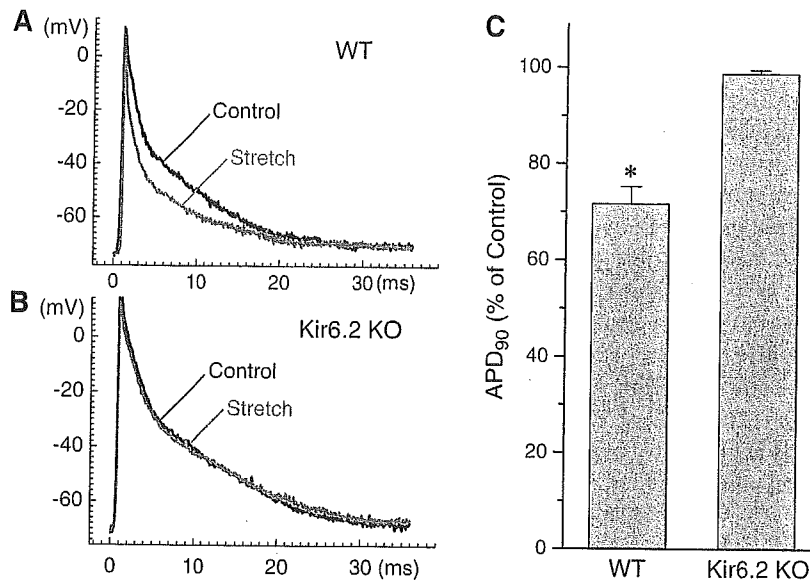
Fig. 5. Representative recording of action potentials before (Control, black) and 5 min after stretch (Stretch, grey) in the atrium of WT (A) and Kir6.2 KO (B) mice. (C) Summarized effects of stretch on the action potential duration. The action potential duration at 90% repolarization (APD_{90}) was measured 5 min after stretch and given as a percentage of the control value. Data represent mean±SEM of 4 experiments for each group. *$p < 0.05$ vs. control.

used to record whole-cell membrane currents and atrial cells were perfused with either isotonic or hypotonic solutions. Fig. 6A shows the representative current traces recorded in response to voltage ramps from -100 to $+50$ mV. In an atrial cell of WT, a hypotonic stretch of the membrane for 10 min evoked an outward current that could be reduced by the subsequent application of glibenclamide (1 µM). The reversal potential of the glibenclamide-sensitive current,
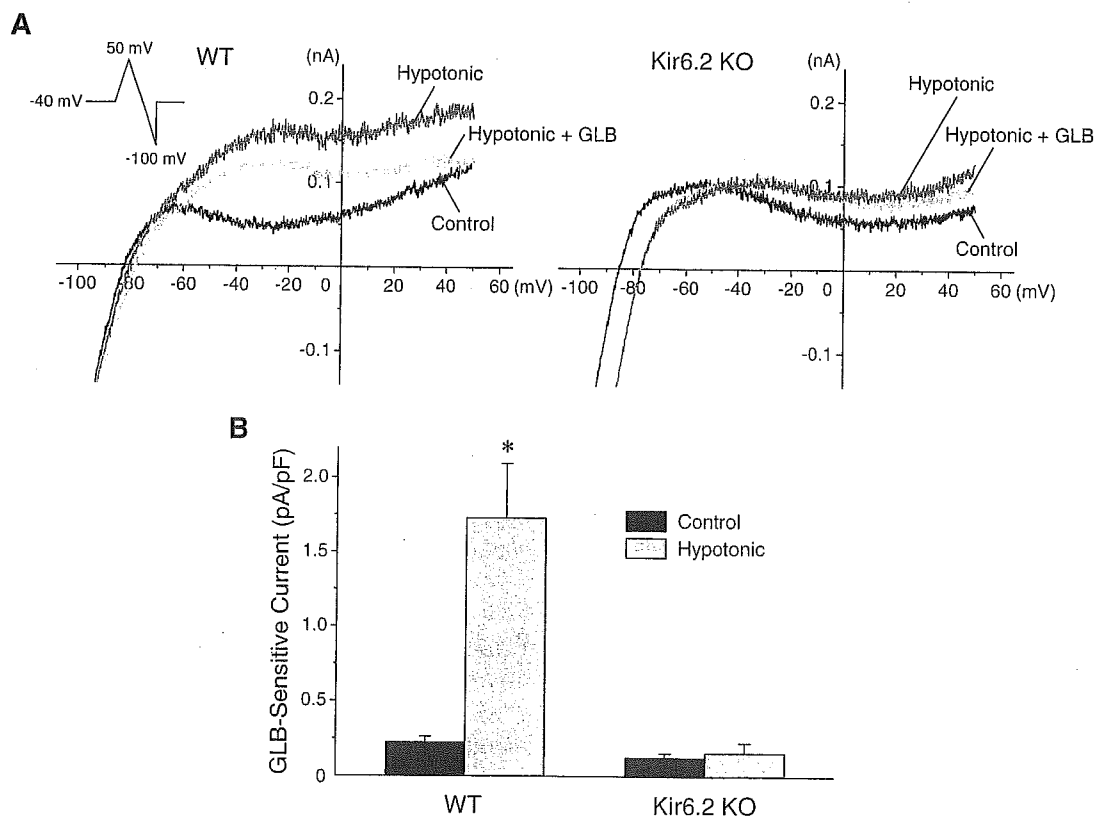

Fig. 6. Activation of the atrial K_{ATP} current by hypotonic stretch. (A) Original whole-cell voltage-ramp currents traces of atrial cells from WT (left) and Kir6.2 KO mice (right). (B) Glibenclamide-sensitive current densities at 0 mV in WT ($n = 4$) and Kir6.2 KO ($n = 4$) atrial cells are summarized. Values are mean±SEM. *$p < 0.05$ vs. control.

which isolated by digital subtraction of the current trace in the presence of glibenclamide from that under hypotonic condition, was close to the K^+ equilibrium potential (~ -80 mV, data not shown). On the other hand, a hypotonic stretch of the membrane slightly increased the outward current in Kir6.2 KO cells, but this current was not blocked by glibenclamide. As summarized in Fig. 6B, hypotonic stretch of WT cells significantly increased the glibenclamide-sensitive outward current at 0 mV from 0.23 ± 0.03 to 1.73 ± 0.36 pA/pF ($n = 4$, $p < 0.05$). However, in Kir6.2 KO cells, a glibenclamide-sensitive outward current was not evoked under hypotonic stretch (from 0.13 ± 0.03 to 0.16 ± 0.07 pA/pF, $n = 4$, $p = 0.66$). These results indicate that K_{ATP} channel current is activated by hypotonic stretch of the membrane in atrial cells from WT but not Kir6.2 KO mice.

4. Discussion

4.1. Kir6.2 forms the pore of atrial K_{ATP} channels

A previous study using primary cultured neonatal rat atrial cells suggested that molecular composition of atrial K_{ATP} channels may be different from that of ventricular K_{ATP} channels based on the functional and pharmacological profiles [17]. In the present study, however, a glibenclamide-sensitive K_{ATP} channel current could be observed during metabolic inhibition in atrial cells of WT but not Kir6.2 KO mice (Fig. 1A and B). In addition, we found that the unitary conductance of single K_{ATP} channel current in WT mouse atrial cells (71.6 ± 1.7 pS, $n = 7$, Fig. 1C) was close to that of ventricular cells (75.9 ± 1.3 pS, $n = 7$, data not shown). Therefore, it can be concluded that Kir6.2 is essential for the function of mouse atrial K_{ATP} channels and Kir6.2 KO mice are potentially useful to examine whether K_{ATP} channel modulates the secretion of ANP.

4.2. K_{ATP} channel modulates ANP secretion in vivo and in vitro

It is acknowledged that ANP is stored as pro-ANP within the granules of cardiomyocytes and released in response to atrial stretch [18,19]. Pro-ANP is cleaved during the release process by a cardiac protease, corin, to form the biologically active C-terminal ANP [20]. Here we examined, in vivo and in vitro, whether K_{ATP} channel is crucial for the regulation of ANP secretion. Plasma volume expansion was used as a means of producing release of the cardiac ANP granules in vivo. There were no significant differences in the basal plasma ANP levels (Fig. 2) between WT and Kir6.2 KO mice. After the initial volume expansion (200 μl/h/g for 30 min), MAP in WT and Kir6.2 KO mice increased to similar extents (Fig. 3), suggesting that the volume expansion seemed to be equally effective in both WT and Kir6.2 KO mice. In WT mice, however, volume expansion was

insufficient to cause a significant increase in plasma ANP concentration. Despite a rather mild volume expansion, a significant increase of plasma ANP concentration was observed in Kir6.2 KO mice (Fig. 2). ANP promotes diuresis/natriuresis and reduces vascular tone [8]. Consequently, hypotension might occur in Kir6.2 KO but not in WT mice (Fig. 3), accompanied by an excessive secretion of ANP.

ANP secreted into the bath from atrial tissue in vitro was small and $\leq 30\%$ of preparations exceeded the threshold for detection in control conditions. However, 4 of 8 preparations (50%) from Kir6.2 KO mice exceeded the threshold for detection after mechanical stretch and the ANP concentration was greater than that of WT atria (Fig. 4). Thus, in vitro study using isolated atria was consistent with the findings in vivo. Since ANP content of WT atria was not statistically different from Kir6.2 KO atria, in vivo and in vitro studies suggest that Kir6.2 KO mice are susceptible to stretch-induced secretion of ANP. Furthermore, given the fact that an excess of ANP produced hypotension in Kir6.2 KO mice, it is reasonable to suppose that activation of K_{ATP} channels is a mechanism for feedback inhibition of stimulated ANP release.

4.3. Activation of atrial K_{ATP} channels by mechanical stretch

Based on pharmacological experiments, it has been proposed that K_{ATP} channels regulate ANP secretion [10,11]. In the present study, we found that mechanical stretch shortened the action potential duration in WT atria, but not in Kir6.2 KO atria (Fig. 5). Van Wagoner [9] reported that K_{ATP} channels in rat atrial cells were mechanosensitive and activated by a hypotonic swelling. Later on, Baron et al. [17] also demonstrated a hypotonic-induced activation of the atrial appendage K_{ATP} channel currents. In agreement with previous reports, we could record the glibenclamide-sensitive K_{ATP} channel current in response to a hypotonic stretch in atrial cells of WT but not of Kir6.2 KO mice (Fig. 6). Although we did not investigate the hypotonic stretch-induced ANP secretion, Jiao et al. [11] have demonstrated that a hypotonic swelling increases ANP secretion in rat atrial myocyte culture. Together, these findings suggest that mechanical stimulus of atrial myocytes activates K_{ATP} channel in association with ANP secretion.

4.4. Possible mechanisms underlying K_{ATP} channel-mediated regulation of ANP secretion

Our observations raise the question of how stretch-induced opening of K_{ATP} channels prevents excessive release of ANP. The diagram of Fig. 7 shows the possible mechanism underlying K_{ATP} channel-mediated regulation of ANP secretion. Mechanical stretch in isolated atrial tissues was reported to increase the intracellular Ca^{2+} transients and the late duration of the action potentials, which was ascribed
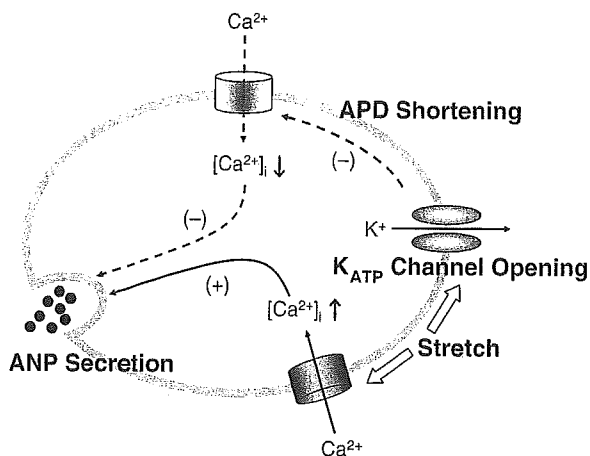
Fig. 7. Hypothetical representation of mechanism by which opening of K_{ATP} channels acts as a negative modulator of ANP secretion. Mechanical stretch in atrial tissue increases the intracellular Ca^{2+} concentration ($[Ca^{2+}]_i$) and thereby stimulates the release of ANP. On the other hand, K_{ATP} channel opens when stretched and decreases $[Ca^{2+}]_i$ by shortening of action potential duration (APD), which in turn inhibits the release of ANP. (+): stimulation, (−): inhibition. (See text for details.)

to the stretch-induced channel activation and resultant augmentation of the Na^+/Ca^{2+}-exchanger inward current [21,22]. It has also been proposed that intracellular Ca^{2+} plays a critical role in ANP secretion from atrial cells and changes of cytosolic Ca^{2+} concentration affect ANP secretion [8,23,24]. Activation of atrial K_{ATP} channels by mechanical stretch may decrease the cytosolic Ca^{2+} concentration by abbreviating the action potentials, which is expected to reduce the time for Ca^{2+} influx via L-type Ca^{2+} channels and to increase the time for Ca^{2+} extrusion through the Na^+/Ca^{2+}-exchange system. Whatever the mechanism involved, the present study clearly demonstrates that K_{ATP} channels negatively regulate ANP secretion from atrial tissues.

4.5. Conclusions

ANP is known to produce a variety of physiological actions such as diuretic, vasodilative [25,26], anti-ischemic [27] and antihypertrophic actions [28]. In the present study we have provided evidence that Kir6.2 is essential for the function of K_{ATP} channel in atrial myocytes and that K_{ATP} channel-dependent mechanism contributes to the regulation of ANP secretion. Recently, a functional study using Kir6.2 KO mice has demonstrated that disruption of K_{ATP} channel function leads to impaired Ca^{2+} handling, cardiac dysfunction and lethal arrhythmias under vigorous sympathetic stimulation, suggesting requirement of K_{ATP} channels for adaptation to physiological stress [7]. Furthermore, it has been reported that in failing hearts the metabolic dysregulation of K_{ATP} channels can occur and resultant loss of protective mechanisms expands the risk of disease progression [29]. Therefore, ANP secretion induced by impaired K_{ATP} channel function may play a compensatory

role by protecting the heart under pathophysiological states. It is likely, however, that under physiological conditions K_{ATP} channel may act as a negative feedback mechanism for the control of ANP secretion.

Acknowledgments

References

[1] Noma A. ATP-regulated K^+ channels in cardiac muscle. Nature 1983; 305:147–8.

[2] Seino S, Miki T. Physiological and pathophysiological roles of ATP-sensitive K^+ channels. Prog Biophys Mol Biol 2003;81:133–76.

[3] Miki T, Nagashima K, Tashiro F, Kotake K, Yoshitomi H, Tamamoto A, et al. Defective insulin secretion and enhanced insulin action in K_{ATP} channel-deficient mice. Proc Natl Acad Sci U S A 1998;95: 10402–6.

[4] Yamada K, Ji JJ, Yuan H, Miki T, Sato S, Horimoto N, et al. Protective role of ATP-sensitive potassium channels in hypoxia-induced generalized seizure. Science 2001;292:1543–6.

[5] Suzuki M, Li RA, Miki T, Uemura H, Sakamoto N, Ohmoto-Sekine Y, et al. Functional roles of cardiac and vascular ATP-sensitive potassium channels clarified by Kir6.2-knockout mice. Circ Res 2001;88:570–7.

[6] Suzuki M, Sasaki N, Miki T, Sakamoto N, Ohmoto-Sekine Y, Tamagawa M, et al. Role of sarcolemmal K_{ATP} channels in cardioprotection against ischemia/reperfusion injury in mice. J Clin Invest 2002;109:509–16.

[7] Zingman LV, Hodgson DM, Bast PH, Kane GC, Perez-Terzic C, Gumina RJ, et al. Kir6.2 is required for adaptation to stress. Proc Natl Acad Sci U S A 2002;99:13278–83.

[8] Roskoaho H. Atrial natriuretic peptide: synthesis, release, and metabolism. Pharmacol Rev 1992;44:479–576.

[9] Van Wagoner DR. Mechanosensitive gating of atrial ATP-sensitive potassium channels. Circ Res 1993;72:973–83.

[10] Kim SH, Cho KW, Chang SH, Kim SZ, Chae SW. Glibenclamide suppresses stretch-activated ANP secretion: involvements of K_{ATP}^+ channels and L-type Ca^{2+} channel modulation. Pflügers Arch 1997; 434:362–72.

[11] Jiao JH, Baumann P, Baron A, Roatti A, Pence RA, Baertschi AJ. Sulfonylurea receptor ligands modulate stretch-induced ANF secretion in rat atrial myocyte culture. Am J Physiol 2000;278:H2028–38.

[12] Xu T, Jiao JH, Pence RA, Baertschi AJ. ATP-sensitive potassium channels regulate stimulated ANF secretion in isolated rat heart. Am J Physiol 1996;271:H2339–45.

[13] Sorota S. Insights into the structure, distribution and function of the cardiac chloride channels. Cardiovasc Res 1999;42:361–76.

[14] Kishimoto I, Dubois SK, Garbers DL. The heart communicates with the kidney exclusively through the guanylyl cyclase-A receptor: acute handling of sodium and water in response to volume expansion. Proc Natl Acad Sci U S A 1996;93:6215–9.

[15] Bilder GE, Siegl PK, Schofield TL, Friedman PA. Chronotropic stimulation: a primary effector for release of atrial natriuretic factor. Circ Res 1989;64:799–805.

[16] Marumo F, Sakamoto H, Ando K, Ishigami T, Kawakami M. A high sensitive radioimmunoassay of atrial natriuretic peptide (ANP) in human plasma and urine. Biochem Biophys Res Commun 1986;137: 231–6.

[17] Baron A, van Bever L, Monnier D, Roatti A, Baertschi AJ. A novel K_{ATP} current in cultured neonatal rat atrial appendage cardiomyocytes. Circ Res 1999;85:707–15.

[18] Kangawa K, Tawaragi Y, Oikawa S, Mizuno A, Sakuragawa Y, Nakazato H, et al. Identification of rat gamma atrial natriuretic polypeptide and characterization of the cDNA encoding its precursor. Nature 1984;312:152–5.

[19] Vuolteenaho O, Arjamaa O, Ling N. Atrial natriuretic polypeptides (ANP): rat atria store high molecular weight precursor but secrete processed peptides of 25–35 amino acids. Biochem Biophys Res Commun 1985;129:82–8.

[20] Yan W, Wu F, Morser J, Wu Q. Corin, a transmembrane cardiac serine protease, acts as a pro-atrial natriuretic peptide-converting enzyme. Proc Natl Acad Sci U S A 2000;97:8525–9.

[21] Laine M, Arjamaa O, Vuolteenaho O, Ruskoaho H, Wechstrom M. Block of stretch-activated atrial natriuretic peptide secretion by gadolinium in isolated rat atrium. J Physiol 1994;480:553–61.

[22] Tavi P, Han C, Weckstrom M. Mechanisms of stretch-induced changes in $[Ca^{2+}]_i$ in rat atrial myocytes: role of increased troponin C affinity and stretch-activated ion channels. Circ Res 1998;83:1165–77.

[23] Schiebinger RJ, Li Y, Cragoe Jr EJ. Calcium dependency of frequency-stimulated atrial natriuretic peptide secretion. Hypertension 1994;23:710–6.

[24] Suzuki E, Hirata Y, Kohmoto O, Sugimoto T, Hayakawa H, Matsuoka H, et al. Cellular mechanisms for synthesis and secretion of atrial natriuretic peptide and brain natriuretic peptide in cultured rat atrial cells. Circ Res 1992;71:1039–48.

[25] Baxter GF. The natriuretic peptides. Basic Res Cardiol 2004;99:71–5.

[26] Ahluwalia A, MacAllister RJ, Hobbs AJ. Vascular actions of natriuretic peptides: cyclic GMP-dependent and -independent mechanisms. Basic Res Cardiol 2004;99:83–9.

[27] Rastegar MA, Vegh A, Papp JG, Parratt JR. Atrial natriuretic peptide reduces the severe consequences of coronary artery occlusion in anaesthetized dogs. Cardiovasc Drugs Ther 2000;14:471–9.

[28] Oliver PM, Fox JE, Kim R, Rockman HA, Kim HS, Reddick RL, et al. Hypertension, cardiac hypertrophy, and sudden death in mice lacking natriuretic peptide receptor A. Proc Natl Acad Sci U S A 1997;94: 14730–5.

[29] Hodgson DM, Zingman LV, Kane GC, Perez-Terzic C, Bienengraeber M, Ozcan C, et al. Cellular remodeling in heart failure disrupts K_{ATP} channel-dependent stress tolerance. EMBO J 2003;22:1732–42.

Plasma low-density lipoprotein reduction and structural effects on coronary atherosclerotic plaques by atorvastatin as clinically assessed with intravascular ultrasound radio-frequency signal analysis: A randomized prospective study

Masaki Yokoyama, MD,[a] Nobuyuki Komiyama, MD, PhD,[b] Brian K. Courtney, MD, PhD,[c] Takashi Nakayama, MD,[a] Susumu Namikawa, MD, PhD,[a] Nehiro Kuriyama, MD, PhD,[a] Tomomi Koizumi, MD, PhD,[a] Mizuo Nameki, MD, PhD,[d] Peter J. Fitzgerald, MD, PhD,[c] and Issei Komuro, MD, PhD[a] *Saitama, Japan*

Background Plaque stabilization by statins is important for reduction of cardiovascular events but has not been demonstrated enough in vivo. We examined whether statins clinically alter the structure of coronary atherosclerotic plaques using intravascular ultrasound (IVUS) radio-frequency (RF) signal analysis.

Methods Fifty consecutive patients undergoing percutaneous coronary intervention were enrolled. Intravascular ultrasound radio-frequency signals were acquired from non–percutaneous coronary intervention-targeted echolucent plaques. The patients were randomly assigned into 2 groups: group S (n = 25) taking atorvastatin 10 mg/d and group C (n = 25) as control. After 6-month follow-up, IVUS-RF signals were sampled at the same plaque sites. Several regions of interest were placed on each plaque. Intravascular ultrasound radio-frequency parameters were blindly calculated in all regions of interests (group S, n = 148; group C, n = 191). Targeted plaque volumes were also measured. Those data were compared between baseline and follow-up.

Results In group S after 6 months, plasma low-density lipoprotein level was significantly decreased (133 ± 13 to 87 ± 29 mg/dL, $P < .0001$), integrated backscatter of IVUS-RF signals was substantially increased (-53.8 ± 4.5 to -51.2 ± 4.9 dB, $P < .0001$), and plaque volume was significantly reduced, whereas no change was demonstrated in group C.

Conclusions These results suggest that statins alter properties as well as volumes of coronary plaques within 6 months, which may be related to plasma low-density lipoprotein reduction. Intravascular ultrasound radio-frequency signal analysis may be useful to evaluate the effects of drugs on stabilization of coronary atherosclerotic plaques. (Am Heart J 2005;150:287.e1-287.e7.)

The rupture of lipid-laden coronary plaques has been put forth as a frequent cause of acute coronary syndrome.[1] Because the so-called vulnerable coronary plaque frequently exists at angiographically mild or minimally stenosed sites, it is important to evaluate

plaque properties and to stabilize the vulnerable plaque even in the angiographically mild stenosis.[2] Lipid-lowering therapy with statins has been proposed to affect the stability of coronary atherosclerotic plaques. Several large trials reported that statins could reduce coronary events in both primary and secondary prevention efforts.[3-9] Studies focused on coronary plaque regression with statins demonstrated that the clinical benefits of avoiding serious cardiac events are more significant than the regression of angiographically detected stenoses.[10] In rabbit studies, statins increased collagen content and decreased lipid deposition, macrophage accumulations, and matrix metalloproteinase activity in an established atheroma.[11,12] All these results suggest that statins do not only reduce plaque size but also stabilize plaques; however, the effect of statins on the histologic composition of human coronary plaque has not been well demonstrated in vivo.

Although conventional intravascular ultrasound (IVUS) imaging can provide real-time cross-sectional gray-scale images of coronary endovascular structures including plaque distribution, it is difficult to accurately identify coronary plaque subtypes such as fatty or fibrous plaques using IVUS gray-scale images.[13,14] We have reported that IVUS radio-frequency (RF) signal analysis is useful to discriminate between fibrous and degenerated tissue in vivo with >90% sensitivity and specificity.[15] In addition, several ex vivo analyses have demonstrated that IVUS-RF parameters such as integrated backscatter (IB) and other RF spectral data are useful to discriminate histologic components in a human coronary plaque.[13,16,17] In the present study, we examined whether statins clinically alter the composition of coronary atherosclerotic plaques of humans by in vivo IVUS-RF analysis.

Methods
Study design and patients

Fifty consecutive patients with stable angina indicated to percutaneous coronary intervention (PCI) were enrolled. Basic inclusion criteria were age <75 years, plasma total cholesterol (TC) level between 170 and 230 mg/dL, and without previous medical treatment of hyperlipidemia. The subjects were randomly assigned into 2 groups: group S consisted of 25 patients taking 10 mg/d of atorvastatin and group C consisted of 25 patients with only dietary modification as controls. The 10 mg/d of atorvastatin to treat hyperlipidemia is a usual and effective dosage for Japanese patients with less body mass than Americans or Europeans. Intravascular ultrasound and RF sampling were performed after PCI, but before randomization, for baseline measurements and again at 6-month follow-up. The patients were seen every month in an outpatient clinic at the Chiba University Hospital.

At baseline, we used IVUS to search for echolucent plaques with IVUS defined by the American College of Cardiology Clinical Expert Consensus Document in the PCI-targeted vessel and other non–PCI-targeted vessels.[18] Candidate plaques were required to demonstrate <50% stenosis by angiographic measurements. Plaques within the arterial segment 10 mm proximal of the PCI-targeted area were excluded to avoid influence on them from the PCI treatment. A total of 71 plaques were targeted for IVUS-RF analysis.

Major exclusion criteria were significant left main disease, unstable angina or acute myocardial infarction within the previous 3 months, or an ejection fraction <40%. Written consent was obtained from each patient for the study and the trial was approved by the institutional review board at Chiba University Hospital and the ethical committee of Chiba University Graduate School.

Intravascular ultrasound imaging and RF sampling

For all IVUS examinations, we used a ClearView Ultra IVUS system (Boston Scientific Corp, Fremont, Calif) with a 3F 40-MHz mechanical transducer catheter (Boston Scientific Corp). After intracoronary injection of nitroglycerin (0.1 mg into right coronary artery and 0.2 mg into left coronary artery),

the IVUS catheter was advanced to the distal portion of the coronary vessel. Motorized pullback of the IVUS catheter was performed at a speed of 0.5 mm/s. Intravascular ultrasound images were recorded in S-VHS videotapes during all IVUS imaging and RF sampling.

Radio-frequency signals were sampled at a single cross section through each target plaque, whereas the IVUS images were simultaneously monitored on an IVUS video screen to confirm the RF sampling sites. The cross section was basically at the site of the largest plaque area within the target plaque. Those RF signals were unprocessed "raw" signals that were completely separated from producing IVUS gray-scale images. The RF signals were digitized at 500 MHz with 8-bit resolution in an online PC with a high-speed A/D converter board (Gage Applied, Inc, Montreal, Canada) and were stored in the PC for subsequent off-line RF analysis. Radio-frequency sampling occurred during the diastolic phase of the cardiac cycle using an electrocardiogram monitor to avoid the influence of cyclic variation of the signals. The position of catheter during RF sampling was recorded by angiography. When RF signals were sampled at 6-month follow-up, extraordinary attention was paid to position an IVUS catheter at the longitudinally and circumferentially same section in the targeted plaque as baseline by using angiography or topographic landmarks of the IVUS video images, as well as distance measurements from major landmarks. Just after RF sampling, the specific profile of RF-signal amplitude related to distance from each catheter-transducer was measured in vitro using a special water tank with a polished glass plate.

Intravascular ultrasound and RF signal analysis

Volumetric measurements and calculation of RF parameters were performed by an experienced IVUS investigator (MY) blinded to treatment assignment while visualizing the baseline and follow-up IVUS video images side by side. Plaque area was measured with a planimetry software TapeMeasure (Indec Co, Sunnyvale, Calif) at 1-mm intervals from 5 mm distal to 5 mm proximal of the RF sampling site. Plaque area was defined as external elastic membrane (EEM) area minus lumen area. Plaque volume was calculated by Simpson's method of integration of the 1-mm-thick disks over the 10 serial plaque areas. Of 71 IVUS targeted plaques, 59 plaques underwent volumetric measurement, whereas accurate IVUS measurements were technically difficult for the remaining 12 plaques because of large calcifications or branch vessels. To assess the reproducibility of IVUS measurements, baseline images of 16 cases were randomly selected and reanalyzed at least 4 weeks after the initial reading. The intraobserver correlation coefficients for plaque volume, lumen volume, and vessel volume were 0.996, 0.998 and 0.998, and the percentage of errors were 0.26% ± 1.06%, 0.51% ± 1.01%, and 0.40% ± 0.86%, respectively.

Each RF data set was composed of 256 vectors over 360° of rotation of the transducer with 4096 samples per vector. A single cross-sectional image was reconstructed. Plaque area was defined as the area between the EEM and the lumen border. The plaque area was divided into 12 regions of interest (ROIs). These ROIs were automatically delineated by the custom-developed software, which divided the plaque area into sectors by using equally spaced radial lines from the center of EEM area (Figure 1).

Figure 1
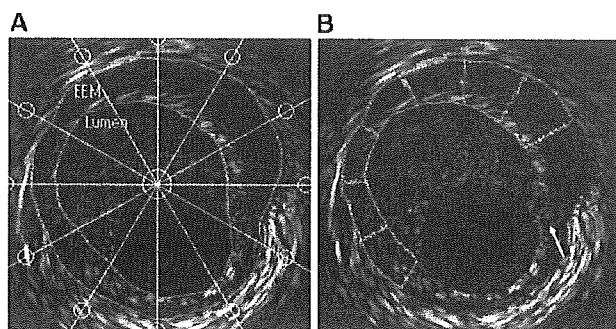
External elastic membrane and lumino-intimal border are lined on 2-dimensional mapping of RF data. Plaque area is divided into 12 ROIs with radial lines shown in panel **A**. Only ROIs with adequate thickness (>0.5 mm) and ROIs without calcification or guidewire artifact (arrow head) are selected for analysis (panel **B**).

Regions of interest with any calcifications, guidewire artifacts, or with a maximal plaque thickness of <0.5 mm were abandoned. In each ROI, time-domain statistical parameters of mean-to-SD ratio (MSR) and skewness, and a frequency-domain power parameter of IB in decibels were calculated in a PC using an originally developed software. Before calculations, the amplitude of the RF signals was corrected by the amplitude-distance profile of each specific catheter-transducer obtained just after each RF sampling procedure. The statistical parameters were based on the probability distribution function of the RF amplitude derived from an envelope of an RF signal. Skewness is the third-order parameter referring to the asymmetry of the distribution. The frequency-domain power parameter was derived from a power spectrum calculated by fast Fourier transformer. The value of IB power in an ROI was calculated according to the following equation:

$$IB = 10 \times \log_{10}(APtissue/Apref) \text{ (dB)}$$

where APtissue is the average power (square volts) in a frequency range of 20-dB bandwidth of a signal from a tissue and APref (square volts) from a polished glass plate as a perfect reflector. The ROIs of each plaque site were matched with their corresponding ROIs at follow-up. Each of the RF parameters was compared between the matched pairs of ROIs at baseline and follow-up. In addition, IB was calculated for sliding windows with 128 data points on each vector of RF signal and presented as a color-coded 2-dimensional map, which was superimposed to a corresponding IVUS cross-sectional image. Those calculations and analysis were made by an investigator (MY) blinded to treatment assignment (by SN and MN) and independently of acquisition of IVUS images and RF signals (by NK).

To assess the reproducibility of RF parameter measurements, the investigator (NK) acquired IVUS images and RF signals at the same sites in 2 independent IVUS procedures during PCI in additional 10 patients who were randomly selected. Another investigator (MY) placed 75-paired ROIs in 10-paired plaque

areas on the reconstructed cross-sectional images acquired in the 2 procedures and calculated the RF parameters in each ROI. The correlation coefficients between the 2 RF sampling and calculating procedures for IB, MSR, and skewness in the paired ROIs were 0.991, 0.972 and 0.982, and the percentage of errors were 0.39% ± 9.78%, 0.57% ± 5.10%, and −1.43% ± 7.81%, respectively.

Statistical analysis

Values are presented as mean ± SD. Statistical analysis was performed with paired t test to compare data between baseline and follow-up, unpaired t test to compare data between groups S and C, or analysis of variance (post hoc Bonferroni) to compare IB changes among 3 classes of % low-density lipoprotein (%LDL) reduction using a commercially available software (StatView version 5.0, ABACUS Inc, Berkley, Calif). A P value <.05 was considered to be significant.

Results

Characteristics of the patients

Of the 50 patients, 8 patients were withdrawn prematurely because of a drug-related increase of serum creatinine level (1 in group S), because of re-PCI for re-stenosis before 6 months, which influenced target plaques (2 in group S and 1 in group C), and because of failure of follow-up for 6 months (2 in group S and 2 in group C). There were no complications resulting from IVUS imaging procedures.

Both groups showed no significant difference with regard to baseline characteristics including clinical histories, concomitant medications, nature of coronary artery disease, the number of studied plaques located in the PCI-targeted artery, and plasma lipid levels (Table I, Figure 2).

Effects on plasma lipid levels

The effects of atorvastatin on plasma lipid levels in 6 months are presented in Figure 2. Atorvastatin induced a marked reduction in TC and LDL cholesterol (LDL-C) levels (198 ± 17 to 156 ± 26 mg/dL and 133 ± 13 to 87 ± 29 mg/dL, respectively, $P < .0001$), whereas high-density lipoprotein cholesterol (HDL-C) level was significantly increased (44 ± 11 to 49 ± 15 mg/dL, $P = .019$) during the 6 months. Percentage of change of TC and LDL during the follow-up ([value at follow-up − value at baseline] / value at baseline × 100 [%]) in group S were −20% ± 17% and −34% ± 20%, respectively. No significant change in TC, LDL-C, and HDL-C levels was observed in group C.

Changes in IB, MSR, and skewness over 6 months

To elucidate whether the atorvastatin treatment changes properties of coronary plaque, we compared RF parameters of 148 ROIs in group S and 191 ROIs in group C (Table II). Mean-to-SD ratio was significantly decreased (1.20 ± 0.30 to 1.14 ± 0.29,

Table I. Baseline characteristics of the patients

Variable	Group S	Group C
n	20	22
Age (y)	62.1 ± 10.2	64.4 ± 8.7
Male sex	18 (90)	20 (91)
Clinical history		
Hypertension	11 (55)	10 (45)
Diabetes mellitus type 2	3 (15)	5 (23)
Current smoking	6 (30)	7 (32)
Concomitant medications		
Aspirin	19 (95)	21 (95)
ACE inhibitor	7 (35)	8 (36)
Angiotensin antagonist	7 (35)	6 (27)
β-Blocker	7 (35)	4 (18)
Calcium antagonist	9 (45)	8 (36)
Nature of coronary artery disease		
Single vessel	18 (90)	19 (86)
Multivessel	2 (10)	3 (14)
Plaques for IVUS measurements (n)	35	36
Location of plaques for IVUS measurements		
LCA	28 (80)	29 (81)
RCA	7 (20)	7 (19)
Plaques in PCI-targeted vessel	16 (46)	19 (53)

Values are mean ± SD or number (percentage) unless otherwise indicated.
ACE, Angiotensin-converting enzyme; LCA, left coronary artery; RCA, right coronary artery.

Figure 2
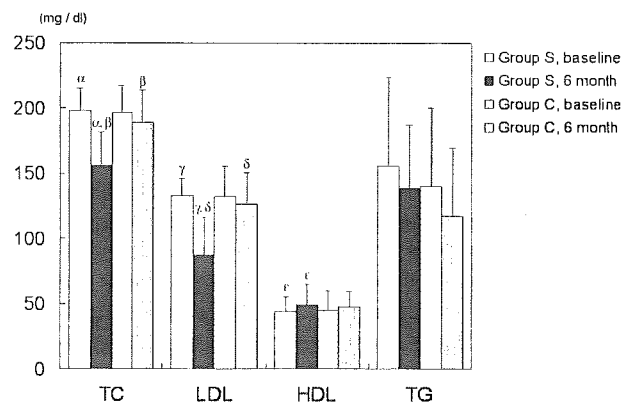
Changes in lipid parameters during the 6-month follow-up in groups S and C are shown. TC and LDL-C are significantly decreased and HDL-C is substantially increased in group S ($^{α,γ}P$ < .0001, $^{β,δ}P$ < .001, ^{ε}P = .019). TG, Triglyceride.

Table II. Radio-frequency parameters derived from IVUS measurements

| Parameter	Group S (n = 148)	Group C (n = 191)	P
IB			
Baseline (dB)	−53.8 ± 4.5	−53.1 ± 4.0	.184
6-m follow-up (dB)	−51.2 ± 4.9	−53.1 ± 4.8	.0001
P	<.0001	.991	
Baseline	1.86 ± 0.79	1.96 ± 1.10	.255
6-m follow-up	2.11 ± 0.78	1.94 ± 0.75	.038
P	.025	.845	
MSR			
Baseline	1.20 ± 0.30	1.24 ± 0.30	.088
6-m follow-up	1.14 ± 0.29	1.21 ± 0.26	.001
P	.040	.298	

Values are mean ± SD.

Figure 3
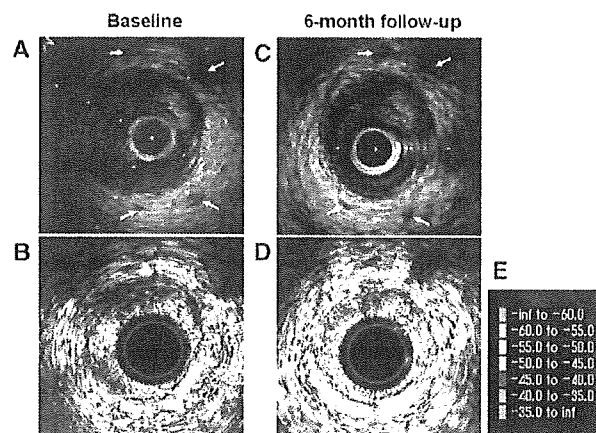
Intravascular ultrasound gray-scale cross-sectional images (upper panels) and color-coded maps reconstructed according to IB values of a coronary plaque (lower panels) in group S are shown. Panels A and B are at baseline and panels C and D are at 6-month follow-up. White arrowheads show side branches as landmarks in A and C to perform IVUS acquisitions at the same section at baseline and at 6-month follow-up. Color codes corresponding to ranges of IB value in decibels are shown in E. Integrated backscatter ranges became greater at 10 to 2 o'clock in the plaque area at the follow-up (panel D) than at baseline (panel B).

P = .040) and skewness was substantially increased (1.86 ± 0.79 to 2.11 ± 0.78, P = .025) during the 6-month follow-up in group S, whereas there was no significant change in those parameters in group C. Integrated backscatter was significantly increased by 2.6 dB (−53.8 ± 4.5 to −51.2 ± 4.9 dB, P < .0001) in group S but not in group C. The increase of IB in

group S could be more clearly recognized by comparison of the color-coded IB maps between baseline and follow-up (Figure 3).

The relation between IB changes and LDL changes over 6 months in group S

There was a good inverse correlation between change of LDL and change of IB values. An increase in IB change was related to %LDL reduction (LDL at baseline − LDL at

Figure 4
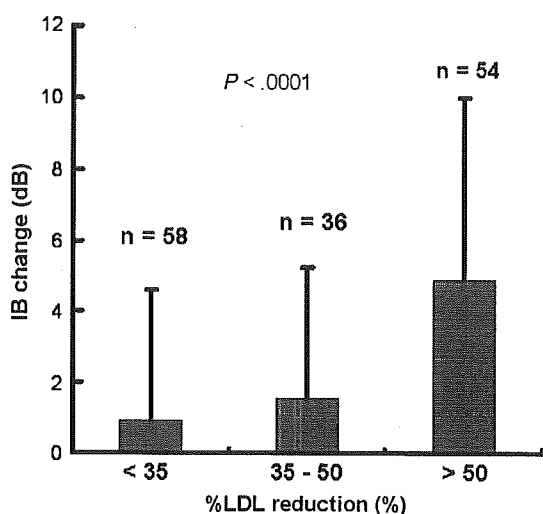
Relation between IB change in ROIs and %LDL reduction during 6 months is demonstrated. The difference of IB change was especially apparent when %LDL reduction was >50%.

Table III. Volume parameters derived from IVUS measurements

	Group S (n = 29)	Group C (n = 30)
Vessel volume		
Baseline (mm^3)	135.5 ± 57.9	102.4 ± 48.1
6-m follow-up (mm^3)	131.1 ± 52.8	102.5 ± 50.1
P	.194	.962
Lumen volume		
Baseline (mm^3)	65.7 ± 27.8	46.6 ± 24.3
6-m follow-up (mm^3)	65.0 ± 25.5	48.3 ± 29.5
P	.816	.408
Plaque volume		
Baseline (mm^3)	69.9 ± 35.0	55.8 ± 27.5
6-m follow-up (mm^3)	66.0 ± 32.1	53.8 ± 25.5
P	.024	.254

Values are mean ± SD.

follow-up / LDL at baseline ×100 [%]) (IB changes 0.92 ± 3.70, 1.56 ± 3.66, 4.91 ± 5.10 dB at %LDL reductions <35, 35-50, >50%, respectively, $P < .0001$). The difference of IB change was most apparent when %LDL reduction was >50% (Figure 4).

Intravascular ultrasound analysis of plaque volumes

Plaque volume was significantly reduced by 3.2% (69.9 ± 35.0 to 66.0 ± 32.1 mm^3, $P = .024$) during the 6 months in group S; however, no significant change was observed in group C. Vessel volume tended to be reduced by 2.9% (135.5 ± 57.9 to 131.1 ± 52.8 mm^3, $P = .194$) in group S (Table III). These results suggest that 6-month treatment with atorvastatin may reduce volumes of coronary atherosclerotic plaques.

Discussion

In the present study, atorvastatin treatment for 6 months induced changes in the acoustic properties of coronary plaques. The correlations between the value of RF parameters and tissue types in atherosclerotic plaques have been shown in several in vivo and ex vivo studies.[13-17] We have already reported that the IVUS-RF parameters were useful to discriminate between American Heart Association type III and type IV/Va human coronary plaques ex vivo.[13] In an in vivo study analyzing tissue samples resected at directional coronary atherectomy, we demonstrated that IB and skewness values were significantly greater in fibrous tissue than in degenerated tissue and that MSR values were

substantially smaller in fibrous tissue than in degenerated tissue.[15] Kawasaki et al[16] reported that IB value was significantly greater in fibrous tissue than in lipid cores by an ex vivo comparison with plaque histology. Fibrous tissues in a coronary plaque contain more collagen fibers, which may reflect RF more than fatty tissues and lead to greater IB values. Furthermore, variance of reflected RF amplitude from each fine tissue component may become greater in fibrous tissue than fatty/degenerated tissue so that it may cause the difference of MSR and skewness between fibrous tissue and fatty/degenerated tissue. Although those studies suggest that sensitive and specific IVUS-RF analysis could discriminate between fibrous and fatty tissues, complete in vivo discrimination of plaque composition is difficult because the classification of fibrous, fibro-fatty, or fatty tissues is an attempt to categorize a continuous spectrum of tissue composition to a small set of classes.[17] In the present study, RF parameters of IB and skewness were significantly increased and MSR was substantially decreased in a group treated with atorvastatin for 6 months. Lipid-lowering therapy increased collagen content and decreased lipid deposition, macrophage accumulation, and matrix metalloproteinase activity in established atherosclerotic plaques in rabbits.[11,12] These findings suggest that the changes of RF parameters reflect some combination of an increase in fibrous tissue and/or a reduction of fatty, degenerated tissue in atherosclerotic plaques.

A correlation between the degree of LDL reduction and the degree of IB change was observed in our study. Many large prevention trials with statins have shown a correlation between the percentage of reduction of cholesterol and reduction of cardiovascular events, and our results may account for the results of the large trials.[19] Schartl et al[20] demonstrated in the GAIN study that the degrees of change in acoustic properties evaluated by gray-scale echogenicity analysis of IVUS video images were significantly different between

2 groups with different degrees of lipid intervention: aggressive lipid intervention to <100 mg/dL LDL and usual lipid-lowering care over 12 months. The result is consistent with the present study. The analysis of RF ultrasound signals provides a more robust framework for this kind of inquiry than gray-scale measurements. Several more parameters can be accurately assessed with IVUS-RF as compared to gray-scale imaging, which is also machine- and user setting–dependent. This may be a reason why IVUS-RF analysis succeeded to demonstrate structural change of coronary atherosclerotic plaques by atorvastatin in a shorter period of 6 months than the previous IVUS gray-scale image analysis as in the GAIN study.

Previous clinical trials have suggested that the stabilizing effects of statin on plaques begin to take place by means of an apparently lower occurrence of ischemic events. In the WOSCOP study and the LIPID trial, according to Kaplan-Meier analysis of time to a definite nonfatal myocardial infarction or death from coronary heart disease, the cumulative risk curves begin to diverge between the pravastatin and placebo groups as early as 6 months after the initiation of treatment.[4,7] Another trial demonstrated that aggressive lipid-lowering with atorvastatin resulted in a lower ischemic event rate after 6 months compared with angioplasty.[21] The LIPS trial demonstrated that treatment with fluvastatin reduces major adverse cardiac events in patients who have undergone PCI. In this trial, major adverse cardiac events–free survival curves began to separate between fluvastatin and placebo after 6 months of follow-up.[9] Those results and observations suggest that statins stabilize coronary plaques within 6 months, which results in apparent reduction of cardiovascular events after 6 months. In addition, the present study revealed that morphologic changes of plaques occur in a relatively short time span of 6 months. The LIPS trial and our present study are similar at the point that cardiovascular events arising from lesions except plaques with severe stenosis are reduced from 6 months of statin treatment.

On the other hand, the dosage of 10 mg/d of atorvastatin in our study might be too small for American or European people to be effective for stabilizing coronary plaques as well as lipid lowering. However, the dosage for Japanese patients should be almost equivalent to a dosage of 20-80 mg/d for Euro-American people with regard to the changes of plasma lipid profiles (averaged LDL reduction of 34%) in 6 months.[19]

In the present study, plaque volume was slightly but significantly decreased after 6-month administration of atorvastatin. There are several recent reports about statin-induced volumetric change of coronary atherosclerotic plaques analyzed with IVUS video images. The REVERSAL study demonstrated that intensive lipid-lowering therapy with atorvastatin for 18 months reduced progression of coronary atherosclerosis and

plaque volume might regress especially in patients with >50% reduction of LDL-C.[22] Jensen et al reported that a significant reduction in coronary plaque volume of 6.3% was observed in patients with stable ischemic heart disease after 12-month administration of simvastatin reducing LDL-C of 42.6%.[23] The ESTABLISH study demonstrated that more reduction of plaque volume of 13.1% was observed in patients with acute coronary syndrome after 6-month administration of atorvastatin reducing LDL-C of 41.7% and suggested that unstable coronary plaques could regress more by aggressive lipid-lowering therapy.[24] Result of the present study may be almost similar to those studies. Because we selected only echolucent plaques, which might include some unstable plaques at baseline, volumetric regression in those plaques could be more easily demonstrated even after only 6-month administration of atorvastatin, reducing LDL of 34%.

In summary, the present study with IVUS-RF analysis suggests a clinically observable mechanism of structural changes as "stabilization" of coronary atherosclerotic plaques after 6-month administration of a statin.

Study limitations

There are several limitations to be taken into account in the present study. First, a small number of patients were enrolled. Second, the RF parameters analyzed in this study do not provide quantitative descriptions of the fibrous or fatty tissue components. They demonstrate trends that are believed to be highly consistent with increased fibrous composition and/or decreased lipid composition. In addition, there was no target plaque with a clearly identified lipid core, even with the use of IVUS-RF. Therefore, it was not possible to provide a validated measure of volumetric reduction of lipid cores. Third, inflammatory responses in a coronary plaque such as migration of macrophages or T lymphocytes, which is thought to be an important factor of plaque vulnerability, cannot be detected by IVUS-RF analysis method to date. Optical coherence tomography and coronary thermography are thought to be invasive diagnostic modalities that can detect and evaluate the inflammatory responses in coronary atherosclerotic plaques.[25,26] Despite these limitations, however, it was possible to observe significant changes that are consistent with known acoustic properties of important components of vascular lesions.

Conclusions

Treatment with atorvastatin altered acoustic properties of coronary atherosclerotic plaques in 6 months. These results may explain one of the mechanisms for statins to prevent ischemic coronary events demonstrated previously in large clinical trials. Intravascular ultrasound radio-frequency signal analysis may be useful

to evaluate the stabilization of coronary atherosclerotic plaques as changes of histologic composition by statin.

References

1. Falk E, Shah PK, Fuster V. Coronary plaque disruption. Circulation 1995;92:657-71.
2. Nobuyoshi M, Tanaka M, Nosaka H, et al. Progression of coronary atherosclerosis: is coronary spasm related to progression? J Am Coll Cardiol 1991;18:904-10.
3. Scandinavian Simvastatin Survival Study Group. Randomized trial of cholesterol lowering in 4444 patients with coronary heart disease. Lancet 1994;344:1383-9.
4. Shepherd J, Cobbe SM, Ford I, et al. Prevention of coronary heart disease with pravastatin in men with hypercholesterolemia. N Engl J Med 1995;333:1301-7.
5. Sacks FM, Pfeffer MA, Moye LA, et al. The effect of pravastatin on coronary events after myocardial infarction in patients with average cholesterol levels. N Engl J Med 1996;335:1001-9.
6. Downs JR, Clearfield M, Weis S, et al. Primary prevention of acute coronary events with lovastatin in men and women with average cholesterol levels: results of AFCAPS/SUB-TexCAPS. JAMA 1998;279:1615-22.
7. Long-Term Intervention with Pravastatin in Ischemic Disease (LIPID) Study Group. Prevention of cardiovascular events and death with pravastatin in patients with coronary heart disease and a broad range of initial cholesterol levels. N Engl J Med 1998;339:1349-57.
8. Riegger G, Abletschauser C, Ludwig M, et al. The effect of fluvastatin on cardiac events in patients with symptomatic coronary artery disease during one year of treatment. Atherosclerosis 1999;144:263-70.
9. Serruys PWJC, de Feyter P, Macaya C, et al. Fluvastatin for prevention of cardiac events following successful first percutaneous coronary intervention. JAMA 2002;287:3215-22.
10. Gotto AM. Lipid lowering, regression, and coronary events. A review of the Interdisciplinary Council on Lipids and Cardiovascular Risk Intervention, Seventh Council Meeting. Circulation 1995;92:646-56.
11. Shiomi M, Ito T, Tsukada T, et al. Reduction of serum-cholesterol levels alters lesional composition of atherosclerotic plaques: effects of pravastatin sodium on atherosclerosis in mature WHHL rabbits. Arterioscler Thromb Vasc Biol 1995;15:1938-44.
12. Aikawa M, Rabkin E, Okada Y, et al. Lipid lowering by diet reduces matrix metalloproteinase activity and increases collagen content of rabbit atheroma. Circulation 1998;97:2433-44.
13. Komiyama N, Berry GJ, Kolz ML, et al. Tissue characterization of atherosclerotic plaques by in intravascular ultrasound radiofrequency signal analysis: an in vitro study of human coronary arteries. Am Heart J 2000;140:565-74.
14. Prati F, Arbustini E, Labellarte A, et al. Correlation between high frequency intravascular ultrasound and histomorphology in human coronary arteries. Heart 2001;85:567-70.
15. Komiyama N, Courtney BK, Toyozaki T, et al. In vivo on-line intravascular ultrasound radio-frequency signal analysis for tissue characterization of coronary atherosclerosis validated by histology of coronary atherectomy tissue specimens. Circulation 2001;104: II-590 [abstract].
16. Kawasaki M, Takatsu H, Noda T, et al. In vivo quantitative tissue characterization of human coronary arterial plaques by use of integrated backscatter intravascular ultrasound and comparison with angioscopic findings. Circulation 2002;105:2487-92.
17. Nair A, Kuban BD, Tuzcu EM, et al. Coronary plaque classification with intravascular ultrasound radiofrequency data analysis. Circulation 2002;106:2200-6.
18. Mintz GS, Nissen SE, Anderson WD, et al. ACC Clinical Expert Consensus Document on Standards for the acquisition, measurement and reporting of intravascular ultrasound studies: a report of the American College of Cardiology Task Force on Clinical Expert Consensus Documents (Committee to Develop a Clinical Expert Consensus Document on Standards for Acquisition, Measurement and Reporting of Intravascular Ultrasound Studies IVUS). J Am Coll Cardiol 2001;37:1478-92.
19. Fager G, Wiklund O. Cholesterol reduction and clinical benefit. Are there limits to expectations? Arterioscler Thromb Vasc Biol 1997;17: 3527-33.
20. Schartl M, Bocksch W, Koschyk DH, et al. Use of intravascular ultrasound to compare effects of different strategies of lipid-lowering therapy on plaque volume and composition in patients with coronary artery disease. Circulation 2001;104:387-92.
21. Pitt B, Waters D, Brown WV, et al. Aggressive lipid-lowering therapy compared with angioplasty in stable coronary artery disease. Atorvastatin versus Revascularization Treatment Investigators. N Engl J Med 1999;341:70-6.
22. Nissen SE, Tuzcu EM, Schoenhagen P, et al. Effect of intensive compared with moderate lipid-lowering therapy on progression of coronary atherosclerosis. A randomized controlled trial. JAMA 2004;291:1071-80.
23. Jensen LO, Thayssen P, Pedersen KE, et al. Regression of coronary atherosclerosis by simvastatin. A serial intravascular ultrasound study. Circulation 2004;110:265-70.
24. Okazaki S, Yokoyama T, Miyauchi K, et al. Volumetric intravascular ultrasound analysis during half a year after coronary event: the ESTABLISH study. Circulation 2004;110:1061-8.
25. Tearney GJ, Yabushita H, Houser SL, et al. Quantification of macrophage content in atherosclerotic plaques by optical coherence tomography. Circulation 2003;107:113-9.
26. Stefanadis C, Diamantopoulos L, Vlachopoulos C, et al. Thermal heterogeneity within human atherosclerotic coronary arteries detected in vivo. A new method of detection by application of a special thermography catheter. Circulation 1999;99:1965-71.

Infertility with Defective Spermiogenesis in Mice Lacking AF5q31, the Target of Chromosomal Translocation in Human Infant Leukemia

Atsushi Urano,[1,2] Masaki Endoh,[3] Tadashi Wada,[3] Yoshihiro Morikawa,[4] Miyuki Itoh,[2] Yuki Kataoka,[5] Tomohiko Taki,[6] Hiroshi Akazawa,[7] Hideaki Nakajima,[8] Issei Komuro,[7] Nobuaki Yoshida,[5] Yasuhide Hayashi,[9] Hiroshi Handa,[3] Toshio Kitamura,[2] and Tetsuya Nosaka[1]*

Division of Hematopoietic Factors,[1] Division of Cellular Therapy,[2] Laboratory of Gene Expression and Regulation, Center for Experimental Medicine,[5] and Center of Excellence,[8] Institute of Medical Science, University of Tokyo, Tokyo 108-8639, Graduate School of Bioscience and Biotechnology, Tokyo Institute of Technology, Midori-ku, Yokohama 226-8501,[3] Department of Anatomy and Neurobiology, Wakayama Medical University, Wakayama 641-8509,[4] Department of Molecular Laboratory Medicine, Kyoto Prefectural University of Medicine Graduate School of Medical Science, Kyoto 602-8566,[6] Department of Cardiovascular Science and Medicine, Graduate School of Medicine, Chiba University, Chiba 260-8670,[7] and Gunma Children's Medical Center, Gunma 377-8577,[9] Japan

AF5q31 (also called MCEF) was identified by its involvement in chromosomal translocation with the gene MLL (mixed lineage leukemia), which is associated with infant acute lymphoblastic leukemia. Several potential roles have been proposed for AF5q31 and other family genes, but the specific requirements of AF5q31 during development remain unclear. Here, we show that AF5q31 is essential for spermatogenesis. Although most AF5q31-deficient mice died in utero and neonatally with impaired embryonic development and shrunken alveoli, respectively, 13% of AF5q31-deficient mice thrived as wild-type mice did. However, the male mice were sterile with azoospermia. Histological examinations revealed the arrest of germ cell development at the stage of spermiogenesis, and virtually no spermatozoa were seen in the epididymis. AF5q31 was found to be preferentially expressed in Sertoli cells. Furthermore, mutant mice displayed severely impaired expression of protamine 1, protamine 2, and transition protein 2, which are indispensable to compact the haploid genome within the sperm head, and an increase of apoptotic cells in seminiferous tubules. Thus, AF5q31 seems to function as a transcriptional regulator in testicular somatic cells and is essential for male germ cell differentiation and survival. These results may have clinical implications in the understanding of human male infertility.

Chromosomal translocation is one of the common pathogenic mechanisms in various human malignancies, particularly in leukemias and lymphomas, and genes located at the breakpoints are involved in disease pathogenesis (21, 59, 60). The mixed lineage leukemia gene MLL (also called HRX, HTRX, and ALL-1) is frequently targeted by chromosomal rearrangements and is associated with clinically aggressive lymphoid and myeloid leukemias which are particularly prevalent in infant leukemias and treatment-related secondary leukemias (2, 18, 24, 64). MLL located on 11q23 is a human homologue of Drosophila trithorax, has a SET domain that normally functions as histone methyltransferase, and is assembled into a super-multiprotein complex with additional chromatin-remodeling components (45, 50, 70). Importantly, most of the leukemic variants of MLL lack the SET domain (7). In Drosophila, genetic evidence suggests that Trithorax controls the expression of homeobox (Hox) genes and regulates embryogenesis (39, 44, 47). In MLL-deficient mice, Hox gene expression initiates normally but is not maintained after 9.5 days postcoitus (dpc), demonstrating the importance of MLL in the mainte-

nance of Hox gene expression (72, 73). Hox genes also play an important role in hematopoietic differentiation, and their expression levels are upregulated in the human leukemias carrying MLL rearrangements (1). An unusual feature of MLL fusion proteins is the large number and diversity of heterologous proteins that fuse with MLL. To date, the MLL locus has been found to be translocated to approximately 40 different genetic loci and at least 30 of the partner genes have been characterized (13, 31). The functions of most MLL partner genes are unknown. Although no consistent homologies or common motifs that are characteristic to all the partner gene sequences have been identified, some are classified into small subgroups according to their sequence homologies. Of interest is that the fusion partner plays an important role in determining disease features.

The (5;11)(q31;q23) translocation is associated with infant acute lymphoblastic leukemia (ALL) (63). This translocation juxtaposes the 5' sequences of the MLL gene to the 3' sequences of the AF5q31 gene and results in the formation of an in-frame MLL-AF5q31 fusion protein which contains the amino-terminal region of MLL, including its AT hooks, methyltransferase domain, and repression domain, and amino acids 351 to 1163 of AF5q31, including the transactivation domain in part and C-terminal homology domain. Based on the significant homology to multiple regions of the predicted AF5q31

* Corresponding author. Mailing address: Institute of Medical Science Division of Hematopoietic Factors, University of Tokyo, 4-6-1 Shirokanedai, Minato-ku, Tokyo 108-8639, Japan. Phone: 81-3-5449-5399. Fax: 81-3-5449-5453. E-mail: tenosaka@ims.u-tokyo.ac.jp.

protein, three other mammalian *AF5q31* homology genes, *AF4*, *LAF4*, and *FMR2*, are known (2). Both *AF4* and *LAF4* have been independently identified as *MLL* partner genes in each case of pediatric ALL (19, 29, 46, 49, 65). In contrast, *FMR2* has not been observed in association with chromosome translocation in leukemia, but congenital mutations in the *FMR2* gene are involved in mild hereditary mental retardation (8, 22, 25). DNA binding and transcriptional properties of AF4, LAF4, and FMR2 suggest that *AF5q31* and other family genes function as nuclear transcription factors (28, 41, 53, 58). Recently, AF5q31 was found to interact with positive transcription elongation factor b (P-TEFb), which activates transcription by RNA polymerase II (RNAPII), leading to the formation of progressive elongation complex (20). Although transfection studies suggested that AF5q31 acts as a repressor of RNAPII transcription, the precise role of AF5q31 in the transcriptional activity of P-TEFb is not known.

AF4 knockout mice demonstrated that AF4 is required for normal lymphopoiesis (34). In the bone marrow of the mutant mice, loss of AF4 function did not disrupt progenitor B-cell development; however, the transition from pre-B cell to the newly generated mature B cell was severely reduced and exhibited defective thymocyte development from a double-negative to a double-positive population. These findings may provide insights into lymphoid leukemogenesis by MLL-AF4. On the other hand, robotic mice carrying autosomal dominant missense mutation in the *AF4* gene have been identified from a large-scale *N*-ethyl-*N*-nitrosurea (ENU) mutagenesis pool (32). As a result, newborn mice developed a severe loss of Purkinje cells of the cerebellum within several weeks after birth and showed a strange ataxic gait. But the thymic double-negative and double-positive populations were not significantly different in the mutant and control mice. Interestingly, AF4 interacts with the E3 ubiquitin ligase SIAH1 and the minimal interaction domain of AF4 to bind to SIAH1 was demonstrated to possess the PXAXVXP motif conserved within *AF5q31* and other family genes (6, 57). A missense mutation V294A in the robotic mice corresponds to Val of the PXAXVXP motif, and the Val mutation of the AF4 protein has been shown to reduce the binding ability to SIAH1 protein significantly, suggesting that the phenotype of the robotic mice is caused by an increased steady-state level of AF4 protein and that all the members of the AF5q31 family are regulated by this interaction (57). Since mutation of the *AF4* gene in the robotic mice occurred upstream of known translocation breakpoints, it is possible that MLL-AF4 may be more stable than AF4. However, the function of AF4 in the robotic mice would not directly account for the leukemogenic potential of MLL-AF4. Thus, there are few available data on the biological and pathological functions for *AF5q31* and other family genes.

We found that *AF5q31* is expressed during mouse embryogenesis at the highest level around 10.5 to 12.5 dpc and is widely expressed in adult mice, especially in Sertoli cells of the testis. This pattern suggests a specific role of AF5q31 during the differentiation of male germ cells. To gain insights into the potential role for AF5q31 in leukemogenesis and normal development, we disrupted the *AF5q31* gene by homologous recombination and examined the mutant phenotype of the mice. Here, we show that AF5q31 deficiency resulted in embryonic and neonatal lethality in most mice but that some survived to

grow properly except for azoospermia, thus raising the possibility that *AF5q31* mutations will be found in some patients with autosomal recessive azoospermia.

MATERIALS AND METHODS

Plasmids. To obtain the mouse *AF5q31* (*mAF5q31*) expression construct, the DNA sequence of full-length m*AF5q31* (GenBank accession number AF190449) was amplified by PCR from Ba/F3 cDNA and subcloned into pcDNA3.1 (Invitrogen) with a FLAG tag.

Antibodies. To prepare the anti-AF5q31 antibody that can recognize both human and mouse AF5q31 proteins, we prepared polyclonal antibodies against the highly conserved transactivation domain of mAF5q31 (E4; 317 to 492 amino acids). DNA sequences corresponding to this region were amplified by PCR and subcloned into pGEX-4T (Amersham Biosciences). Anti-mAF5q31 antisera were raised in rabbits against the purified GST-mAF5q31-E4 (317- to 492-amino acid) fusion protein, depleted of anti-glutathione S-transferase (GST) antibodies, and further affinity purified on an antigen column.

To detect RNAPII, N20 antibody that reacts with both the hyperphosphorylated (IIo) and hypophosphorylated (IIa) forms of RNAPII was purchased from Santa Cruz. H5 and H14 antibodies that recognize Ser2 and Ser5 of the carboxyterminal domain (CTD) phosphopeptides of RNAPII, respectively, were obtained from Covance Co. (Berkeley, CA). In addition, anti-α-tubulin (T-5168; Sigma) was used.

Generation of AF5q31-deficient mice. A phage clone containing an approximately 17-kb DNA fragment was isolated from a mouse 129 SvJ λ genomic library (Stratagene) with the m*AF5q31* cDNA probe. The *AF5q31* targeting vector was constructed by replacing the 5.0-kb HaeII-SspI DNA fragment that contains exon II harboring the initiation codon and exon III with a 1.1-kb fragment of the neomycin-resistant gene (*neo*) cassette of pMC1NeoPolyA (Stratagene) in an antisense orientation. The 2.2-kb fragment of the herpes simplex virus thymidine kinase gene cassette was inserted upstream of the *AF5q31* gene in an antisense orientation for negative selection. The linearized targeting plasmid DNA was electroporated into E14-1 embryonic stem (ES) cells. After double selections with 600 μg/ml G418 (Invitrogen) and 2 μM ganciclovir (Sigma), resistant clones were screened for homologous recombination by Southern blot analysis as described previously (54, 55). In brief, genomic DNA was digested with HindIII, separated by agarose gel electrophoresis, and transferred to a Hybond-N⁺ membrane (Amersham Biosciences). Hybridization was carried out with a 0.3-kb 3′ flanking probe. The targeting frequency was 12/384. ES cells from each of four independent *AF5q31* mutant clones were injected into C57BL/6 blastocysts. The blastocysts were transferred to pseudopregnant ICR foster mothers, and chimeras derived from two independent clones transmitted the mutant allele through their germ line. All animal experiments were done according to the guidelines for animal use issued by the Committee of Animal Experiments, Institute of Medical Science, University of Tokyo.

The genotype was also determined by PCR with Ex Taq (TaKaRa, Otsu, Japan). Genomic DNAs were prepared from mouse tail snips. For the wild-type and mutant alleles of the *AF5q31* gene, an antisense primer specific for the wild-type (5′-GTCTTCACGGTTCATGTTGC-3′) or mutant allele (5′-GCCCG GTTCTTTTTGTCAAG-3′, a sequence in the *neo* gene) was used with a common sense primer (5′-GTGGGTTATGTGCCACCAAA-3′). PCR was done at 96°C for 5 min for initial denaturing, followed by 35 cycles at 96°C for 1 min, 56°C for 1 min, and 72°C for 2 min.

Histology and immunohistochemistry. Formalin-fixed, paraffin-embedded sections (6 μm in thickness) of embryos were stained with hematoxylin and eosin stain. Bouin-fixed, paraffin-embedded sections of testes and epidydimides were stained with hematoxylin and eosin stain. For immunohistochemistry, formalin-fixed, paraffin-embedded sections (6 μm) of testes were deparaffinized, rehydrated, quenched of endogenous peroxidase activity with 3% hydrogen peroxide, and incubated overnight at 4°C with an anti-mAF5q31-E4 antibody. After washing of the sections three times in phosphate-buffered saline, samples were incubated with anti-rabbit immunoglobulin ENVISION horseradish peroxidase (DakoCytomation). The sections were counterstained with hematoxylin.

Northern blot analysis and PCR with reverse transcription (RT-PCR). Mouse multiple tissue blot (Clontech) was hybridized with the ³²P-labeled m*AF5q31* full-length cDNA probe followed by rehybridization with a mouse *AF4*, *LAF4*, and *FMR2* probe and a human glyceraldehyde-3-phosphate dehydrogenase (GAPDH) cDNA probe, as described previously (55, 56). Mouse embryo full-stage blot (Seegene) was hybridized with the m*AF5q31* cDNA probe. The mouse *AF4* and *LAF4* cDNA probes were obtained by PCR amplification from a mouse

thymus cDNA library and the mouse *FMR2* cDNA probe from a mouse brain cDNA library. The human GAPDH cDNA probe was described previously (56). The following oligonucleotide primers specific to mouse *AF4*, *LAF4*, and *FMR2* were used: for *AF4*, 5'-CCTGCTTCGAATCAGAGAGA-3' (sense) and 5'-CA TCCTTAGTCTGGTGAGCT-3' (antisense); for *LAF4*, 5'-GGAGGAAAGAG CGAGAAAGA-3' (sense) and 5'-CCCTCTCCATATTGCACACT-3' (antisense); and for *FMR2*, 5'-GCAGTGTCACTATGAACAAG-3' (sense) and 5'-CCAGGTGCTTGCACTGTAAA-3' (antisense).

To confirm the gene disruption of m*AF5q31*, total RNAs from mouse embryonic fibroblasts (MEFs) obtained from 13.5-dpc embryos and maintained in Dulbecco's modified Eagle medium containing 10% fetal bovine serum were isolated with Trizol reagent (Invitrogen). Total RNA (3 μg) was reverse transcribed using Superscript reverse transcriptase II (Invitrogen) with random primers in a total volume of 20 μl. One μl of this reaction mixture was used as a template for PCR amplification with Ex Taq (TaKaRa) in the following condition: at 96°C for 5 min for initial denaturing, followed by 35 cycles at 96°C for 30 s, 56°C for 30 s, and 72°C for 1.5 min. The following oligonucleotide primers specific to *AF5q31* exons I to IV and GAPDH for a control were used: for *AF5q31* exons I to IV, 5'-GAAATGGTTCGGGCCTAGCG-3' (sense) and 5'-CTACACAGCTTACATCACCA-3' (antisense), and for GAPDH, 5'-ACCAC AGTCCATGCCATCAC-3' (sense) and 5'-TCCACCACCCTGTTGCTGTA-3' (antisense).

To assess the expression levels of several genes in testis, RT-PCR analyses were performed on total RNAs derived from the testes of 12-week-old AF5q31$^{+/+}$, AF5q31$^{+/-}$, and AF5q31$^{-/-}$ male mice and 9-week-old WBB6F1-W/W^v male mice (Japan SLC) using the same methods as in MEFs. The following oligonucleotide primers specific for *TP1*, *TP2*, *Prm1*, *Prm2*, *Tpap*, *RT7*, *Hsc70t*, *Mcs*, *Pgk2*, *Camk4*, *CREM*, *TRF2*, *RARα*, *RXRβ*, *AR*, *FSH-R*, *LH-R*, and *GATA1* were used: for *TP1*, 5'-ATGTCGACCAGCCGCAAGCT-3' (sense) and 5'-TCACAAGTGGGATCGGTAAT-3' (antisense); for *TP2*, 5'-GCCTCAAAG TCACACCAGTA-3' (sense) and 5'-ACTTGTATCTTCGCCCTGAG-3' (antisense); for *Prm1*, 5'-ATGCTGCCGCAGCAAAAGCA-3' (sense) and 5'-CAC CTTATGGTGTATGAGCG-3' (antisense); for *Prm2*, 5'-ATGGTTCGGCTACC GAATGAG-3' (sense) and 5'-TTAGTGATGGTGCCTCCTAC-3' (antisense); for *Tpap*, 5'-GGCTCTTACCGATTAGGAGT-3' (sense) and 5'-AGTTACCC GGCAACCGTTAA-3' (antisense); for *RT7*, 5'-TGCCTGTGTGACTACAAG CT-3' (sense) and 5'-AGTACGTCACGTCCTTCTCA-3' (antisense); for *Hsc70t*, 5'-CCATGAATCCCCAGAACACT-3' (sense) and 5'-ATGACACCTG CATCCTTGGT-3' (antisense); for *Mcs*, 5'-ACCATGTTGCCCACCTAAAC-3' (sense) and 5'-TCTCCAGAGTTTGGCCAGAT-3' (antisense); for *Pgk2*, 5'-C TGTTGCTGATGAGCTCAAG-3' (sense) and 5'-ACTCCGACCATAGAACT GTG-3' (antisense); for *Camk4*, 5'-TCTCTCACACCCGAACATCA-3' (sense) and 5'-GGTTCCACACACTGTCTTCA-3' (antisense); for *CREM*, 5'-ACTTT CCTCTGATGTGCCTG-3' (sense) and 5'-CTTGCGAGTTGCTTCTTCTG-3' (antisense); for *TRF2*, 5'-TGCTTTGGAGGGAGCAAATG-3' (sense) and 5'-AGTTCAGGTTCATAGCTGGC-3' (antisense); for *RARα*, 5'-TTGAGAAGG TTCGCAAAGCG-3' (sense) and 5'-AGGTCAGTGTGTCTTGCTCA-3' (antisense); for *RXRβ*, 5'-AGACTGTACAGTGGACAAGC-3' (sense) and 5'-TG GCAGATGTTAGTCACTGG-3' (antisense); for *AR*, 5'-ACCCTATCCCAGT CCCAATT-3' (sense) and 5'-GATGGGCAATTTTTCCTCCG-3' (antisense); for *FSH-R*, 5'-CGGAACGCCATTGAACTGAG-3' (sense) and 5'-CAAAGCT CAGTCCCATGAAG-3' (antisense); for *LH-R*, 5'-TGCACTCTCCAGAGTTG TCA-3' (sense) and 5'-TCTTCGAAACATCTGGGAGG-3' (antisense); and for *GATA1*, 5'-CAGGTTTCTTTTCCTCTGGG-3' (sense) and 5'-AAAGGACTG GGAAAGTCAGC-3' (antisense).

To monitor the expression of *AF5q31* in the juvenile mice testes at various stages, RT-PCR analyses were done on total RNAs derived from C57BL/6 male mice (Japan SLC) at various ages, using the same methods as in MEFs. The sequence within the *AF5q31* exons V to VIII was amplified with the primers 5'-CGGCTATTCATACACCATGC-3' (sense) and 5'-CTCCCTCACTGTTAT GGTGT-3' (antisense).

Terminal deoxynucleotidyltransferase-mediated dUTP nick end labeling (TUNEL) assay. Formalin-fixed, paraffin-embedded testis sections (6 μm) of 12-week-old mice were prepared, and apoptotic cells were detected in situ using ApoAlert DNA fragmentation assay kits (Clontech). The cells were counterstained with 4',6-diamidino-2-phenylindole [DAPI].

Western blot analysis. An equal amount of total cell lysates from MEFs (10 μg/lane) was separated in 4 to 20% gradient polyacrylamide gels. Proteins were transferred onto a nitrocellulose membrane. The blot was incubated with the primary antibody at room temperature for 1 h and with a horseradish peroxidase-conjugated secondary antibody at room temperature for 1 h. Enhanced chemiluminescence Western blotting detection reagents (Amersham Biosciences) were used for detection.

Assessment of serum hormone levels. The blood of male AF5q31$^{+/+}$, AF5q31$^{+/-}$, and AF5q31$^{-/-}$ mice (<24 weeks) was drawn by cardiocenthesis and stored on ice for 30 min. After 10 min of centrifugation at 800 × g for 10 min, the serum was collected and stored at −80°C until analysis. The levels of serum testosterone, luteinizing hormone (LH), and follicle-stimulating hormone (FSH) were measured by SRL Co. (Tokyo, Japan).

Fertility assessment. The reproductive capacities of 9-week-old male AF5q31$^{+/+}$, AF5q31$^{+/-}$, and AF5q31$^{-/-}$ mice were investigated by mating one male with two 8-week-old C57BL/6j females for 2 weeks, as described previously (10, 26). Female mice were checked for vaginal plugs each morning, and litter sizes were recorded on delivery after three successive matings.

Evaluation of epididymal sperm. The cauda epididymides were removed and minced in 0.1 ml of motile buffer (120 mM NaCl, 5 mM KCl, 25 mM NaHCO$_3$, 1.2 mM KH$_2$PO$_4$, 1.2 mM MgSO$_4$, 1.3 mM CaCl$_2$). The tissues were incubated at 37°C for 5 min to allow sperm to disperse, as described previously (48).

Generation and purification of the recombinant proteins. Human *AF5q31* cDNA (63) was subcloned into pBacPAK8 vector (BD Biosciences) with a hemagglutinin (HA) tag on the N terminus and a FLAG tag on the C terminus. AF5q31 was expressed in Sf9 cells by using a BacPAK baculovirus expression kit (BD Biosciences) according to the manufacturer's instructions. Sf9 cells were solubilized in lysis buffer (50 mM Tris-Cl [pH 7.5], 150 mM NaCl, 1 mM EDTA, 1.0% Triton X-100) supplemented with protease inhibitor cocktails (Sigma). The extract was loaded onto an anti-FLAG M2 agarose (Sigma) column equilibrated with TBS buffer (50 mM Tris-Cl [pH 7.5], 150 mM NaCl), and bound proteins were eluted with TBS buffer supplemented with 0.2 mg/ml FLAG peptide (Sigma). Proteins in the elution were loaded onto an anti-HA 3F10 affinity matrix (Roche) column equilibrated with TBS buffer containing 0.1% NP-40, and bound proteins were eluted with HGKEN buffer (20 mM HEPES-NaOH [pH 7.9], 20% glycerol, 100 mM KCl, 0.2 mM EDTA, 0.1% NP-40) supplemented with 1 mg/ml HA peptide (Roche). Proteins in the eluate were further separated on a Mono Q column (Amersham Biosciences) equilibrated with HGKEN buffer containing 5 mM β-mercaptoethanol and 0.5 mM phenylmethylsulfonyl fluoride by elution with a linear gradient from 200 mM to 400 mM KCl. Each fraction was dialyzed against HGKEN buffer containing 1 mM dithiothreitol and 1 mM phenylmethylsulfonyl fluoride. GST-CTD and P-TEFb were purified as described previously (66, 67).

CTD kinase assay. GST-CTD was incubated with purified P-TEFb and each recombinant AF5q31 fraction in the presence of 60 μM ATP containing [γ-^{32}P]ATP in transcription buffer for 10 min at 30°C as described previously (66, 67). Reaction products were subjected to 4 to 20% gradient polyacrylamide gel electrophoresis followed by autoradiography.
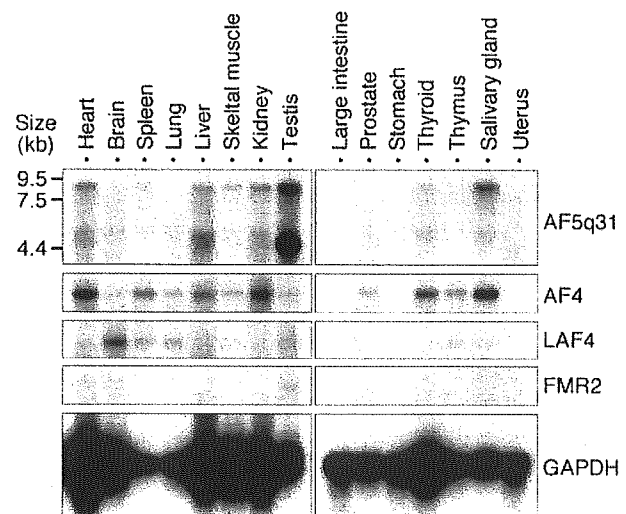

FIG. 1. Expression profiles of mouse *AF5q31* and *AF5q31* family genes in adult normal tissues. Northern blot analysis of poly(A) RNAs (2 μg/lane) from normal mouse tissues. The blot was hybridized to radioactive mouse *AF5q31*, *AF4*, *LAF4*, and *FMR2* probes. As a control, the same blot was rehybridized with a GAPDH probe.